LUT UNIVERSITY
LUT School of Energy Systems
LUT Mechanical Engineering

Giota Goswami

ESTIMATION OF TIRE-ROAD FORCES USING A MULTIBODY BICYCLE MODEL

Examiner(s): Professor Aki Mikkola
Professor Jussi Sopanen

ABSTRACT

LUT University
LUT School of Energy Systems
LUT Mechanical Engineering

Giota Goswami

Estimation of Tire-Road Forces using a Multibody Bicycle Model

Master's thesis

2019

70 pages, 26 figures and 2 tables

Examiners: Professor Aki Mikkola
Professor Jussi Sopanen

Keywords: Multibody dynamics, bicycle, vehicle stability, tire-force estimation

Vehicle handling systems are used to assist drivers in keeping proper control of the vehicle in hazardous situations. They take input from various sensors about the vehicle and road conditions and correcting them accordingly. Current research in this field involve the prediction of tire-road forces which is an important parameter needed for these vehicle handling systems. One of the methods used to predict these forces is the design of a virtual sensor that uses actual sensors to measure certain parameters combined with a mathematical model to derive the values for the desired forces. A multibody bicycle model to estimate tire-road forces is proposed in this research work. The four-rigid-body Whipple model has been used with appropriate selection of coordinates and frames. Kinematic analysis has been performed to obtain the velocities and accelerations of the bicycle. Inverse dynamic analysis has been performed by taking geometric coordinate inputs from the rider's actions on the bicycle. These inputs were fed into the equations of motion to obtain the Lagrange multipliers which showed the values of the reaction forces acting on the tire along with the driving forces.

The estimated tire-road forces match the expected behavior according to the rider's actions and the bicycle can be seen simulating an accurate representation of the real motion. Experimental validation of the tire-forces was initially within the scope of the work. However, due to the inability to measure lateral forces with the current setup it has been moved to the future scope of this topic. The future scope also includes elimination of some assumptions in the model such as zero-slip and point-contact between wheels and ground. The addition of a dynamic observer following the expansion of the model to a four-wheel model has also been discussed as a future scope. The multibody bicycle model provides a good starting point for developing accurate and inexpensive virtual sensors for tire-force estimation suitable for application in vehicle handling and stability systems.

ACKNOWLEDGEMENTS

I would like to thank Professor Aki Mikkola and Professor Jussi Sopanen for giving me the opportunity to carry out this research work. Their guidance in this work was invaluable. This research could not have been completed without their constant encouragement and emphasis on my clear understanding of the multibody model. I would like to thank José L. Escalona for providing me the MATLAB script of the multibody bicycle model which forms the foundation of this research. I am also grateful towards Adam Kłodowski who helped me understand and use the experimental setup.

Giota Goswami

Giota Goswami
Lappeenranta 18.12.2018

TABLE OF CONTENTS

LIST OF SYMBOLS AND ABBREVIATIONS

$\langle X\ Y\ Z \rangle$	Global frame of reference
$\langle \bar{X}_A\ \bar{Y}_A\ \bar{Z}_A \rangle$	Body frame of reference of rolling disk
$\langle x_i\ y_i\ z_i \rangle$	Body frame of reference for body *i* of bicycle
$\langle x_{i1}\ y_{i1}\ z_{i1} \rangle$	First intermediate frame of reference for bicycle
$\langle x_{i2}\ y_{i2}\ z_{i2} \rangle$	Second intermediate frame of reference for bicycle
$\boldsymbol{a}_G^i$	Acceleration of body *i* of bicycle
$\boldsymbol{A}_{disk}$	Rotation matrix of disk
$\boldsymbol{A}^i$	Rotation matrix of body frame of body *i* of bicycle
$\boldsymbol{B}^i$	Jacobian of the rolling-without-slipping constraints of body *i* of bicycle
C	Point of contact between bicycle rear wheel and ground
$\boldsymbol{C}$	Vector of total set of constraints applied on bicycle
C_{1disk}	First holonomic constraint on rolling disk
C_{2disk}	Second holonomic constraint on rolling disk
$\boldsymbol{C}_{disk}$	Vector of total set of holonomic constraint on rolling disk
$C_{nh1disk}$	First non-holonomic constraint on rolling disk
$C_{nh2disk}$	Second non-holonomic constraint on rolling disk
$\boldsymbol{C}_{nhdisk}$	Vector of total set of non-holonomic constraint on rolling disk
$\boldsymbol{C}_{qdisk}$	Jacobian matrix of rolling disk constraints
$\boldsymbol{C}_{\boldsymbol{q}}^{con}$	Jacobian matrix of contact constraints of bicycle
$\boldsymbol{C}^{con}$	Vector of total set of contact constraints of bicycle
$C^{con}{}_1$	First contact constraint of bicycle
$C^{con}{}_2$	Second contact constraint on bicycle
$\boldsymbol{C}_{\boldsymbol{q}}^{mob}$	Jacobian matrix of mobility constraints of bicycle
$\boldsymbol{C}^{mob}$	Vector of total set of mobility constraints of bicycle
$\boldsymbol{C}^{rws}$	Vector of total set of rolling-without-slipping constraints of bicycle
$\boldsymbol{C}_{\boldsymbol{q}}^{rws}$	Jacobian matrix of rolling-without-slipping constraints of bicycle
$C^{rws}{}_1$	First rolling-without-slipping constraint of bicycle wheels
$C^{rws}{}_2$	Second rolling-without-slipping constraint of bicycle wheels
$C^{rws}{}_3$	Third rolling-without-slipping constraint of bicycle wheels

$C^{rws}{}_4$	Fourth rolling-without-slipping constraint of bicycle wheels
$\boldsymbol{C}^{rws,i}$	Vector of total set of rolling-without-slipping constraints of body *i* of bicycle
D	Contact-point between front wheel and ground
$\boldsymbol{D}_h$	Jacobian of holonomic constraints of bicycle
$\boldsymbol{E}$	Time derivative of mobility constraints of bicycle
F_{xC}	Force acting on x_C coordinate of bicycle
F_{yC}	Force acting on y_C coordinate of bicycle
g	Acceleration due to gravity
$\overline{\boldsymbol{g}}^i$	Jacobian of vector of angular velocity of body *i* of bicycle
$\boldsymbol{G}_i$	Center of mass of bicycle body *i*
$\overline{\boldsymbol{G}}^i$	Jacobian of the orientation of body frame of body *i* of bicycle
$\boldsymbol{h}^i$	Jacobian of the absolute velocity vector of body *i* of bicycle
$\boldsymbol{H}^i$	Jacobian of the position of body frame of body *i* of bicycle
i	Number of body in bicycle
$\overline{\boldsymbol{I}}^i$	Inertia of body *i* of bicycle
m_{disk}	Mass of rolling disk
m^i	Mass of body *i* of bicycle
$\boldsymbol{M}$	Mass matrix of bicycle
$\boldsymbol{M}_{disk}$	Mass matrix of disk
M_β	Moment about β angle of bicycle
M_γ	Moment about γ angle of bicycle
M_ϕ	Moment about ϕ angle of bicycle
M_ϵ	Moment about ϵ angle of bicycle
M_θ	Moment about θ angle of bicycle
M_ξ	Moment about ξ angle of bicycle
M_ψ	Moment about ψ angle of bicycle
N	Point of contact between rolling disk and ground
$\boldsymbol{P}^i$	Vector of the weight of body *i* of bicycle
P	An arbitrary point on front wheel of bicycle
$\boldsymbol{q}$	Vector of selected bicycle coordinates
$\dot{\boldsymbol{q}}$	Vector of velocities of selected bicycle coordinates
$\ddot{\boldsymbol{q}}$	Vector of accelerations of selected bicycle coordinates

$\boldsymbol{q}_{disk}$	Vector of selected rolling disk coordinates
$\boldsymbol{Q}_{cdisk}$	Product of Jacobian matrix and accelerations of disk
$\boldsymbol{Q}_{edisk}$	Vector of generalized externally applied forces for disk
$\boldsymbol{Q}_{ext}$	Vector of generalized external forces of bicycle
$\boldsymbol{Q}_{grav}$	Vector of generalized gravity forces of bicycle
$\boldsymbol{Q}_{v}$	Quadratic velocity vector of bicycle
$\boldsymbol{Q}_{vdisk}$	Quadratic velocity vector for disk
r_{disk}	Radius of rolling disk
$\boldsymbol{r}_{D}$	Position vector of point *D* in global frame
$\boldsymbol{r}_{pdisk}$	Position vector of any arbitrary point on disk in global frame
$\bar{\boldsymbol{r}}_{G_i}$	Distance between centers of mass of body *i* and body *i-1*
$\bar{\boldsymbol{r}}^{i}{}_{P}$	Position of any arbitrary point *P* in body *i* of bicycle
R	Radius of bicycle wheels
$\boldsymbol{R}_{A_{disk}}$	Global position of center of mass of disk
$R_{A_{Xdisk}}$	Global x-coordinate of center of mass of disk
$R_{A_{Ydisk}}$	Global y-coordinate of center of mass of disk
$R_{A_{Zdisk}}$	Global z-coordinate of center of mass of disk
$\boldsymbol{R}^{i}$	Position of body frame of body *i* of bicycle
$\boldsymbol{R}^{\mathbf{2}}_{\boldsymbol{G_2}}$	Position of center of gravity of rear wheel of bicycle
t	Time taken
$\boldsymbol{t}_{D}$	Tangent vector at point *D* in global frame
$\boldsymbol{t}^{i}{}_{P}$	Tangent vector at any arbitrary point *P* in body *i* of bicycle
T	Kinetic energy of bicycle
$\overline{\boldsymbol{U}}_{pdisk}$	Position of any arbitrary point on disk
$\boldsymbol{v}_{c}$	Velocity of point *C*
$\boldsymbol{v}_{D}$	Velocity of point *D*
$\boldsymbol{v}_{G_2}$	Velocity of point G_2
$\boldsymbol{v}^{i}_{G}$	Velocity of center of gravity of body *i* of bicycle
$\boldsymbol{v}^{*}_{G_i}$	Virtual magnitude of velocity of body *i* of bicycle
V	Forward velocity of bicycle
V_{disk}	Forward velocity of disk

$\dot{W}^{*}_{grav}$	Virtual magnitude of power of bicycle
x_C	Global x-coordinate of position of bicycle rear wheel contact point *C*
y_C	Global y-coordinate of position of bicycle rear wheel contact point *C*
α_B	Baumgarte stabilization factor alpha
$\overline{\boldsymbol{\alpha}}^{i}$	Angular acceleration of body *i* of bicycle
β_B	Baumgarte stabilization factor beta
β	Rear frame pitch angle of bicycle
$\dot{\beta}$	Velocity of rear frame pitch angle of bicycle
$\ddot{\beta}$	Acceleration of rear frame pitch angle of bicycle
γ	Steering angle of the bicycle
$\dot{\gamma}$	Velocity of steering angle of bicycle
$\ddot{\gamma}$	Acceleration of steering angle of bicycle
γ^{exp}	Experimental steering angle of bicycle
ϵ	Rolling angle of bicycle front wheel
$\dot{\epsilon}$	Velocity of rolling angle of bicycle front wheel
$\ddot{\epsilon}$	Acceleration of rolling angle of bicycle front wheel
θ	Lean (roll) angle of bicycle
$\dot{\theta}$	Velocity of lean (roll) angle of bicycle
$\ddot{\theta}$	Acceleration of lean (roll) angle of bicycle
θ_{disk}	Angle of rotation of body frame about the y-axis
θ^{exp}	Experimental lean angle of bicycle
$\boldsymbol{\lambda}$	Vector of Lagrange multipliers of bicycle
λ_1	First Lagrange multiplier of bicycle
λ_2	Second Lagrange multiplier of bicycle
λ_3	Third Lagrange multiplier of bicycle
λ_4	Fourth Lagrange multiplier of bicycle
λ_5	Fifth Lagrange multiplier of bicycle
λ_6	Sixth Lagrange multiplier of bicycle
λ_7	Seventh Lagrange multiplier of bicycle
λ_8	Eighth Lagrange multiplier of bicycle
λ_9	Ninth Lagrange multiplier of bicycle

$\boldsymbol{\lambda}_{disk}$	Vector of Lagrange multipliers for disk
ξ	Angle made by radius containing point *D* with $x_5$body frame
$\dot{\xi}$	Velocity of angle made by radius containing point *D* with $x_5$body frame
$\ddot{\xi}$	Acceleration of angle made by radius containing point *D* with $x_5$body frame
ϕ	Heading (yaw) angle of bicycle
$\dot{\phi}$	Velocity of heading (yaw) angle of bicycle
$\ddot{\phi}$	Acceleration of heading (yaw) angle of bicycle
ϕ_{disk}	Angle of rotation of body frame about x-axis
ψ	Rolling angle of bicycle rear wheel
$\dot{\psi}$	Velocity of rolling angle of bicycle rear wheel
$\ddot{\psi}$	Acceleration of rolling angle of bicycle rear wheel
ψ_{disk}	Angle of rotation of body frame about y-axis
ψ^{exp}	Experimental rolling angle of rear wheel of bicycle
ϕ	Heading (yaw) angle of bicycle
$\dot{\phi}$	Velocity of heading (yaw) angle of bicycle
$\ddot{\phi}$	Acceleration of heading (yaw) angle of bicycle
ϕ_{disk}	Angle of rotation of body frame about x-axis
$\boldsymbol{\omega}^i$	Angular velocity of body *i*
$\bar{\boldsymbol{\omega}}_G^i$	Angular velocity vector of body *i* of bicycle

ABS	Anti-lock Braking System
BMW	Bavarian Motor Works
CAN	Controller area network
DAE	Differential algebraic equations
DSC	Driving Stability Control
ESP	Electronic Stability Program
IMU	Inertial Measurement Unit
NSK	Nippon Seikō Kabushiki-gaisha
ODE	Ordinary differential equation
SUV	Sports Utility Vehicle
TCS	Traction Control System
TPMS	Tire-Pressure Monitoring System

USA	United States of America
VSA	Vehicle Stability Assist

1 INTRODUCTION

Today vehicles are growing rapidly in numbers. Numerous types of vehicles suitable for many different terrains are being developed. The greater challenges in vehicle design these days are safety, stability and motion-control. ABS (Anti-lock Braking System), TCS (Traction Control System), ESP (Electronic Stability Program) and TPMS (Tire-Pressure Monitoring System) are some of the systems used to ensure proper control of vehicles. The prime focus is on driver assistance systems to ensure safety and improve ride quality.

Driver assistance systems aim to improve safety of vehicles by reducing the burden on drivers. Features like collision avoidance, cruise control, automated lane keeping and safety event recorders are provided in these systems. Stability control systems function in hazardous conditions to avoid loss of control of vehicles. They stop vehicles from drifting, spinning, skidding and rolling over. Figure 1 shows how a vehicle behaves differently with the same steering input on roads with different friction coefficient. Due to the curvature of the road the lateral forces experienced by the vehicle will be different in each case resulting in spinning or skidding. This kind of mishap is avoided using yaw stability control. Ride quality can also be improved by implementing control systems in the vehicle's suspension which compensate the destabilizing forces. (Rajamani, 2014, pp. 1-11.)

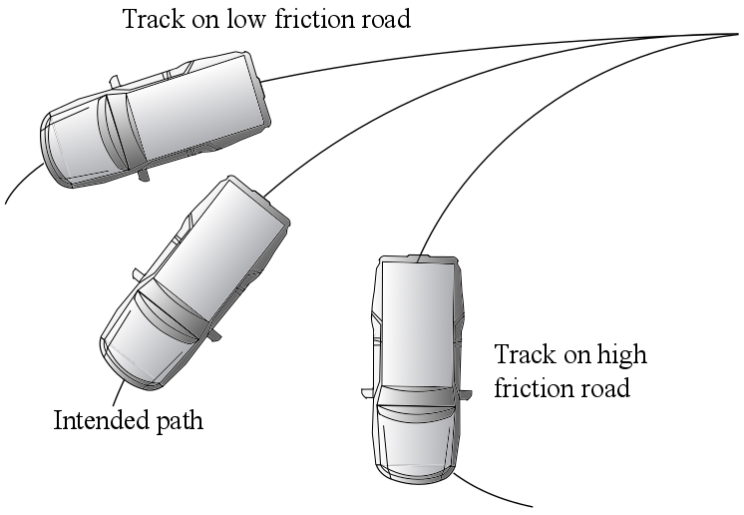

Figure 1. A vehicle behaves differently with the same steering input on roads with different friction coefficient (mod. Rajamani, 2014, p. 3).

These vehicle handling control systems achieve traction control, anti-slip control and yaw stability by taking inputs from various sensors in the vehicle and correcting anomalies faster than the human driver. Of these inputs the most important ones are wheel velocity, acceleration, yaw rate, steering angle and tire-road forces. Knowledge of forces acting on vehicles is required to determine their dynamic behavior. Many properties and variables such as road profile and tire-road friction have to be known to calculate these forces. With the use of various sensors to record these parameters the control systems can get accurate data and improve the safety and ride quality of the vehicle.

1.1 Background

Yaw control systems have been implemented in commercial vehicles since 1995 with the Mercedes ESP, closely followed by the Cadillac Stabilitrak system in 1996. They use sensors detecting steering position, wheel speeds, lateral acceleration, yaw rate and pressure sensors to find the difference between the path intended by the driver and the actual yaw rate and make the necessary corrections with differential braking (Ghoneim et al., 2000, pp. 124-144). Chevrolet developed its vehicle dynamic control system called C5 Corvette Active Handling in 1998. The system uses steering sensor, lateral acceleration sensor, yaw rate sensor, hydraulic modulator valve, differential pressure switch for the brake system and brake pressure transducer. While the steering and speed sensors help determine the desired rate of yaw, the sensor detecting lateral acceleration helps in surface estimation and bank angle compensation (Hoffman and Rizzo, 1998, pp. 1-3).

Honda introduced the VSA (Vehicle Stability Assist) to the market in 1998. It was designed to predict impending loss of tire grip by monitoring the longitudinal and lateral accelerations, individual wheel speed, rate of steering and yaw. Using this sensed data it estimates the lateral forces, lateral acceleration, coefficient of tire-road friction and tire side-slip angles as shown in Figure 2 (Kin et al., 2003, pp. 71-79). BMW (Bavarian Motor Works) also introduced the DSC (Driving Stability Control) system to its 5-series in 1998. It creates a simulation model of the vehicle based on sensors monitoring speed of wheels, steering rate, lateral forces, yaw and pressure. Difference of actual behavior of the vehicle compared to the simulation model indicates understeering or oversteering which the DSC corrects (Leffler et al., 1998, pp. 1-3).

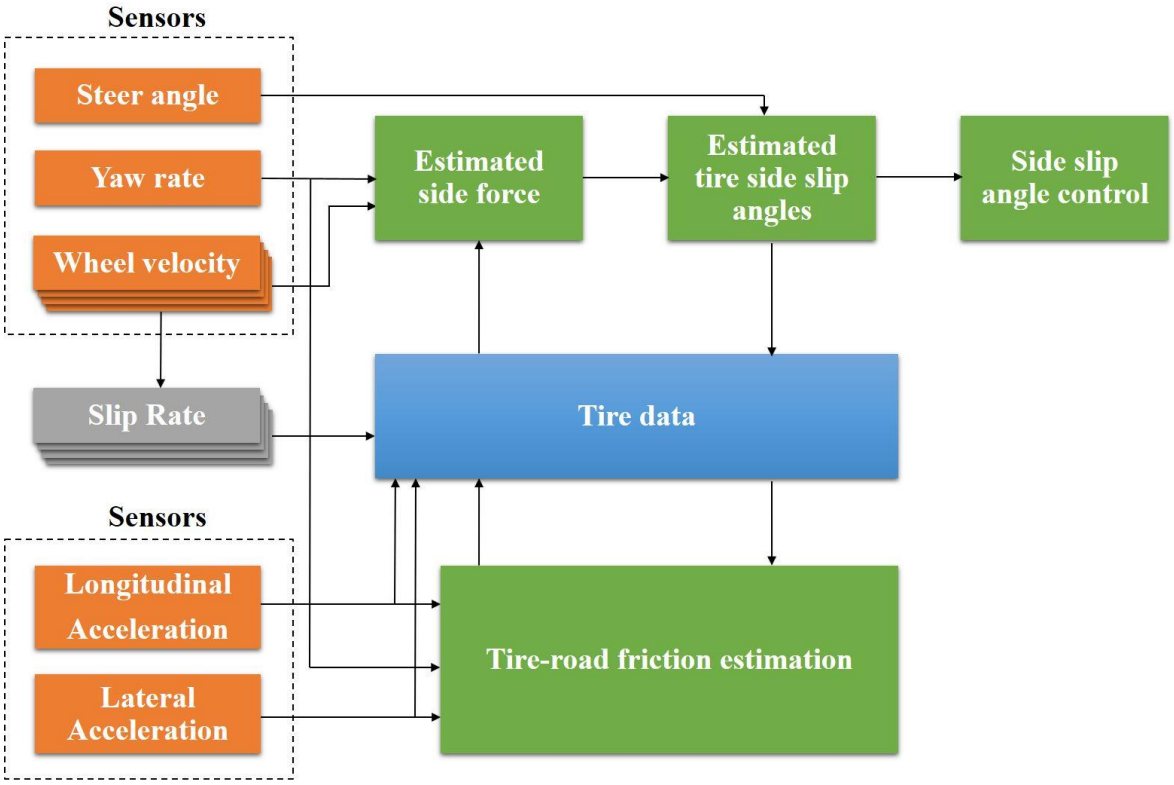

Figure 2. Honda VSA basic estimation logic (mod. Kin et al., 2003, p. 73).

In 2001, BMW launched the Dynamic Drive in its 7-series. It is an active stabilizer bar system which prevents the vehicle from rolling in a corner in addition to yaw stabilization. Sensors are integrated to the Dynamic Drive's hydraulic valve block. They include lateral acceleration and steering angle sensors which are fed into a dynamic observer. The observer then predicts the stabilizing torque to be applied by the stabilizer bar on the suspension to counter the vehicle's rolling tendency (Strassberger and Guldner, 2004, pp. 28-29).

As the trend in these commercialized control systems suggest, there is a shift from feedback control using sensors to prediction and control using simulations in these systems. The reason for that is higher accuracy and economical design. One of the key parameters to control stability while cornering is the tire-road force in lateral direction which simulation models can estimated. When a dynamic observer is added to the simulation model higher accuracy levels can be achieved in the estimation of lateral forces. There is a growing trend in research in this field as shown in Figure 3 which plots the number of research documents with the keywords "tire-force" and "estimation" from 1992 to 2018 found in the Scopus

database (Scopus, 2018). Figure 4 shows that most of these documents are conference papers and journal articles.

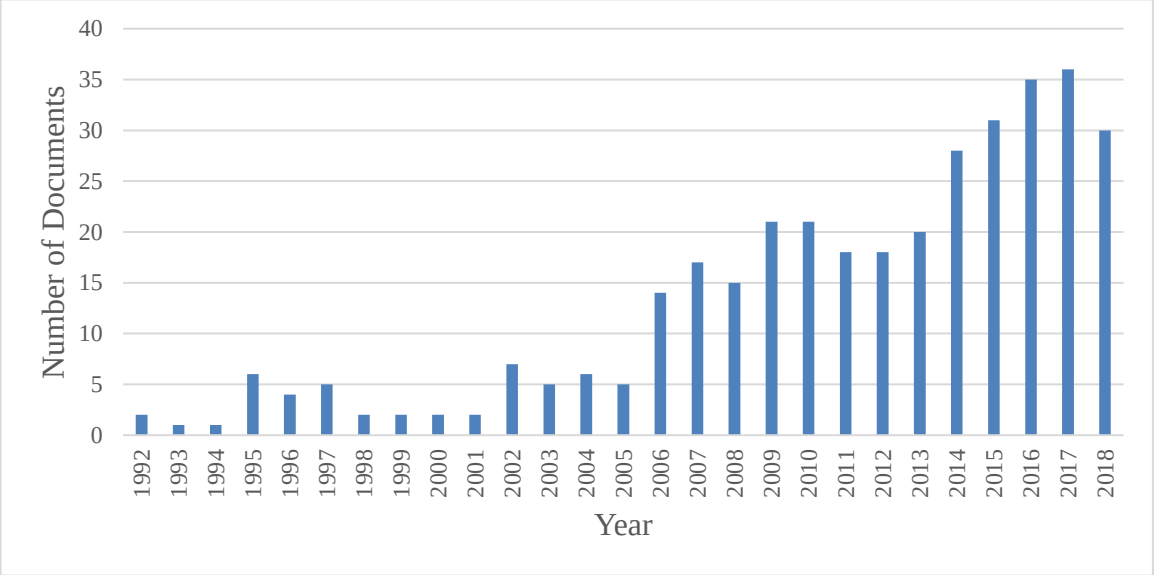

Figure 3. Number of research documents with the keywords "tire-force" and "estimation" from 1992 to 2018 found in Scopus database (Scopus, 2018).

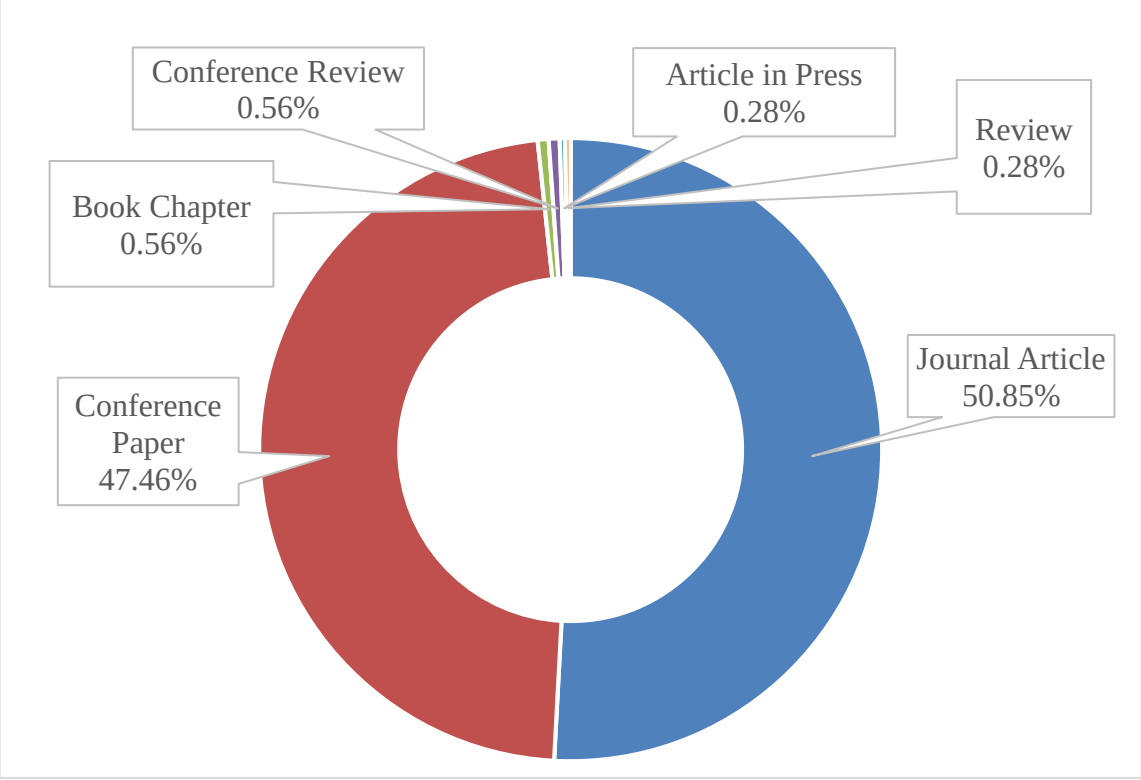

Figure 4. Type of research documents with the keywords "tire-force" and "estimation" from 1992 to 2018 found in Scopus database (Scopus, 2018).

Simulation models are developed by mathematically describing the dynamic vehicle motion with minimal input parameters. This motion is governed by equations of motion which are derived without prior knowledge of the tire and road conditions, vehicle parameters or even the driving forces. Only the geometric parameters of the vehicle which can be recorded with simple and inexpensive sensors are required for such models (Rajamani, 2014, pp. 1-11). Models with low complexity, like two-wheeled bicycle models can also be used as a starting point to develop kinematic models of complex vehicles. Wang and Qi (2001, pp. 3320-3325) use a "Bicycle model" to derive the kinematic model of a vehicle steered by four wheels and develop an algorithm to plan its trajectory. These advantages of simulation based predictive models have made them the highlight of ongoing research in the field of vehicle handling systems.

1.2 Recent works

Mathematical models used to determine tire-road forces have been a topic of extensive research for a long time. Bakker et al. (1987, pp. 190-204) mathematically represented the behavior of vehicle tires while cornering and braking. While the presented formula gives accurate side force, brake force and self-aligning torque characteristics, it requires many coefficients describing tire-road conditions to be measured. A TCS was designed by Lee and Tomizuka (2003, pp. 37-47) for longitudinal control considering the tire-road conditions explicitly. It was verified by a simulation model of a vehicle assuming the bicycle model (dynamics assumed to be identical on both sides of the vehicle) where experimental data from Bakker et al. (1987, pp. 190-204) was used in the tire models. The simulation used in Lee and Tomizuka (2003, pp. 37-47) is based on many assumptions and its accuracy is highly dependent on the tire model. Ono et al. (2003, pp. 1361-1370) proposed a friction force estimation method between the tire and road by estimating extended brake stiffness from the wheel velocities. The method was experimentally verified. Boukattaya et al. (2018, pp. 1-28) achieved external force estimation of a mobile non-holonomic manipulator using only measurements of position and velocity from simple encoders. They developed an adaptive law for external force estimation using which trajectory control of the manipulator can also be achieved. A real-time estimator of vehicle velocity based on wheel velocity measurements and motor torque was developed by Nam et al. (2015, pp. 6820-6840) as part of a wheel slip control system. It uses a driving forces observer. Sanjurjo et al. (2018, pp. 210-228)

combined multibody simulations and indirect extended Kalman filters to develop state and force observers. These observers were implemented on multibody models of three and four bar mechanisms using position, velocity and acceleration sensors.

There has been a steady growth in the use of observers, especially Kalman filters (Grewal et al., 1995, p. 1983), on multibody models of vehicles to derive tire-road forces. Ray (1995, pp. 117-124) implemented the extended Kalman filter in the estimation of lateral and longitudinal tire-forces and histories of state on a vehicle model having nine degrees of freedom without knowing the tire parameters or road properties. The Bicycle model as shown in Figure 5 was adopted for the four wheel vehicle neglecting roll of the vehicle and sensors like accelerometers, tachometers and rate gyroscopes were used. On application of the estimation method on a simulated braking system using simple slip control the Kalman filter appeared to be very effective in tire force estimation (Ray, 1995, pp. 117-124). Ray (1997, pp. 1819-1833) used extended Kalman-Bucy filter on a vehicle model having eight degree of freedom mounted with sensors estimating friction coefficient of the road, motion and tire-road forces on a surface of asphalt. In this method it is not required to know the road characteristics or even tire-force model beforehand. Verification of the method was done by comparison between simulation and field test data (Ray, 1997, pp. 1819-1833). Baffet et al. (2009, pp. 1255-1264) created an observer of sliding mode to calculate tire-road forces using which cornering stiffness and sideslip angle are estimated by an extended Kalman filter. The vehicle dynamic model is based on the bicycle model. The lateral and longitudinal acceleration, steering angle, yaw rate and angular velocities of the wheels are taken from sensors. A car with Correvit sensors for velocity and sideslip angle measurement and dynamometric hubs for actual force measurements was used to gather experimental data to compare with the estimations obtained. The results displayed the potential of two-block estimations - first block estimating tire-forces and second block using the forces in an adaptive tire-force model to estimate sideslip angles (Baffet et al., 2009, pp. 1255-1264). Doumiati et al. (2009, pp. 4804-4809) proposed and compared two observers using unscented Kalman filter and extended Kalman filter. The observers estimate lateral tire-road forces and sideslip angle. The experimental car's ABS system provided the lateral and longitudinal acceleration, steering angle, yaw rate, suspension deflection and angular velocities of the wheels as inputs to the dynamic model. Actual values of lateral tire-road forces and sideslip angle taken from Correvit sensors and dynamometric hubs validated the

observer estimations and showed the potential of observers to replace expensive sensors (Doumiati et al., 2009, pp. 4804-4809). Cho et al. (2010, pp. 638-649) developed an estimation strategy for lateral and longitudinal tire-road forces using a simplified wheel dynamics model in combination with a random-walk Kalman filter. Sensor measurements required in the model include brake pressure, wheel velocities, yaw rate, lateral and longitudinal acceleration. The steps involved are subsequent estimations of vertical tire-road force, shaft torque, longitudinal and lateral tire-road force and finally combined tire-force. Implementation of this estimator on a unified chassis control system showed good performance in simulation (Cho et al., 2010, pp. 638-649).

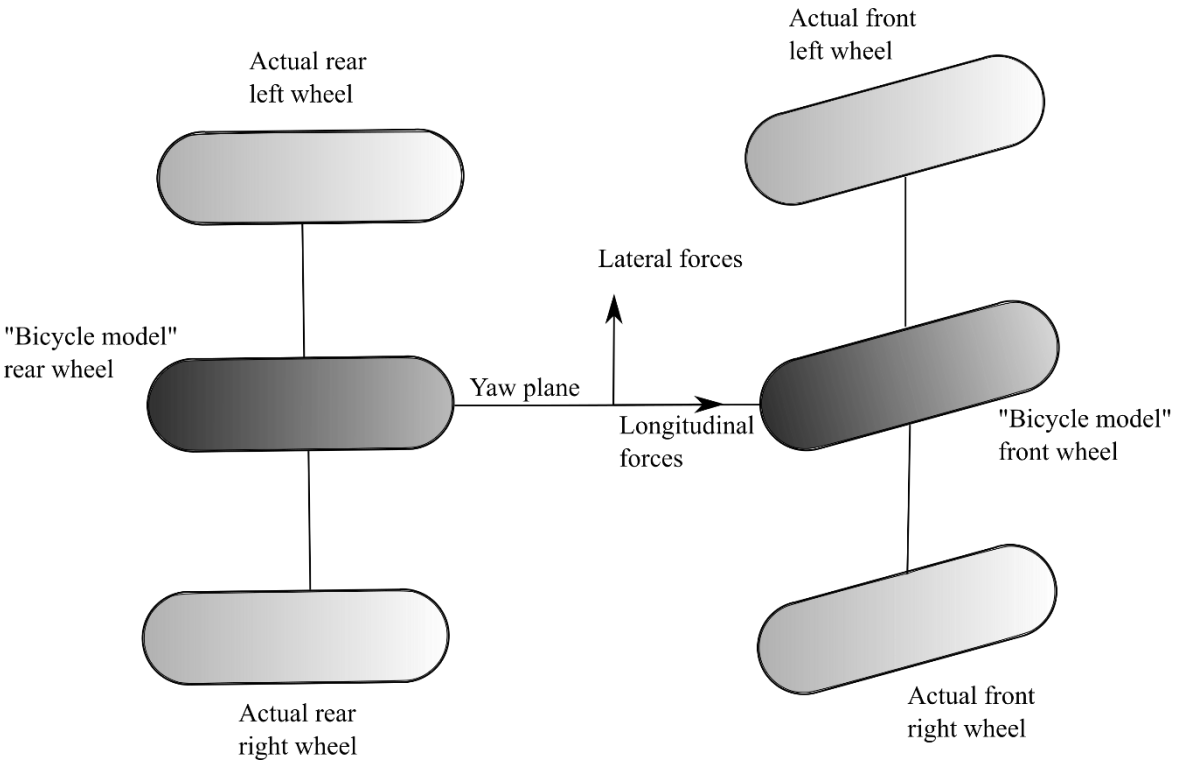

Figure 5. Bicycle model adopted from four wheel model by assuming two wheels on the yaw plane (mod. Ray, 1995, p. 118).

Researches have also been conducted to determine the practical use of force sensors in combination with observers and multibody models in commercial vehicles for tire-force estimation. Nam et al. (2012, pp. 1972-1985) and Nam et al. (2013, pp. 988-1000) developed novel methods of sideslip angle estimation that used a bicycle model for a four wheeled vehicle and a lateral force sensor called the Multisensing Hub (MSHub) invented by NSK (Nippon Seikō Kabushiki-gaisha) Ltd (NSK Ltd, 2014, pp. 21-22). While the method used

by Nam et al. (2012, pp. 1972-1985) also estimates the tire cornering stiffness and uses an extended Kalman filter technique, the method used by Nam et al. (2013, pp. 988-1000) also estimates roll angle and is based on the algorithm of recursive least squares combined with Kalman filter. The MSHub is a compact and low-cost sensor which calculates radial and axial loads by sensing the wheel revolution speeds. These sensor-based estimation methods performed better when compared to kinematics-based methods (Nam et al., 2012, pp. 1972-1985). However, the feasibility of these sensor-based models have not been elaborately analyzed in these studies.

Many other models have been developed aiming to achieve higher levels of accuracy of tire-force estimations or targeting specific types of vehicles. Rezaeian et al. (2015, pp. 2231-2241) proposed a tire-force estimator that is robust against variations in vehicle mass using unscented Kalman filter and extended random-walk Kalman filter. One observer for each wheel is used in the model which also estimates vehicle mass. This kind of estimator would be useful in transportation vehicles like trucks. Here again the vehicle was reduced to a bicycle model with sensor inputs of acceleration in all directions, driving and braking torque, wheel angular velocity and pitch, roll and yaw rates. The estimator was validated by performing critical maneuvers exciting lateral dynamics of an experimental vehicle with sensors. Errors between measured and estimated values of lateral tire-forces ranged from 7.2% to 13.54% (Rezaeian et al., 2015, pp. 2231-2241). The novel method proposed by Jung and Choi (2018, pp. 2934-2944) focuses on tire-force estimations of all-wheel-drive vehicles simultaneously reflecting both slipping rates and clutch lockup. A bicycle model was used for the dynamics with a interacting multiple model filter. The model uses inputs like accelerations, torques and angular velocities of the wheels provided by the CAN (controller area network) bus of the vehicle. The proposed method was compared with a single model Kalman filter estimator and was proved to be robust against sensor noise (Jung and Choi, 2018, pp. 2934-2944).

The methods of tire-force estimation studied in the literature can be grouped into three categories – tire-force models that use road characteristics and tire parameters, simulation models in combination with state and force observers and sensor-based models in combination with state and force observers. Figure 6 outlines the basic structure of these methods. Determination of the accuracy of these methods would require an in-depth

analysis. However, methods using road and tire parameters have the obvious disadvantage of difficulty in measurement of the parameters while sensor-based models pose feasibility issues in commercialized vehicles. The use of simulations with observers comes out as the most appropriate alternative due to their capability to serve as virtual sensors. A virtual sensor measures an immeasurable quantity by feeding available measured quantities into a dynamic system model forming a closed loop observer (Doumiati et al., 2009, pp. 4804-4809). The efficacy of these observers or virtual sensors depend highly on the accuracy of the system model.

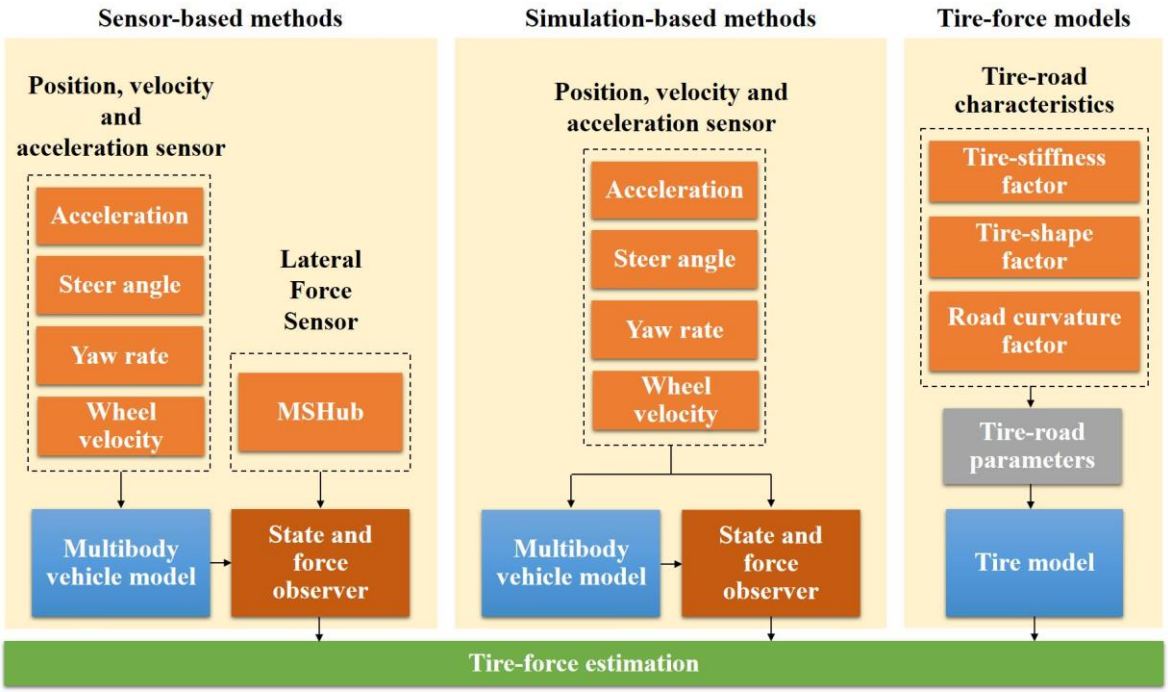

Figure 6. Basic structure of different tire-force estimation methods.

In most of the simulation models referred above, four wheeled vehicles have been simplified into the bicycle model which brings both front wheels and both rear wheels into the yaw plane as one front wheel and one rear wheel. This model often includes assumptions like neglect of the roll motion which is crucial to four wheeled vehicle dynamics. Multibody models of actual bicycles, however, can include many dynamic properties for accurate simulation and the development of these models have been going on for over a century making current models highly evolved and realistic. The Whipple (1899, pp. 312-321) model which consists of four rigid bodies connected by three revolute joints – the front wheel, the handlebar, the rear frame and the rear wheel – is most commonly used in works related to

bicycle dynamics (Figure 7). Schwab et al. (2005, pp. 511-521) derived the linearized equations of motion of a bicycle using the Whipple model at high speed ranges to establish a benchmark. Limitations of this benchmark model were pointed out by Sharp (2008, pp. 1-24) showing the loss of certain dynamic properties in the benchmark model due to its simplification. Dao and Chen (2012, pp. 853-868) used parameters from another benchmark model developed by Meijaard et al. (2007, pp. 1955-1982) representing a more realistic bicycle suitable for measuring dynamic data to design a non-linear dynamic model. In 2013 Schwab and Meijaard (2013, pp. 1059-1090) tracked the numerous extensions to the Whipple model over the past decade aimed at correcting the rigid-rider bicycle model. The review noted the use of inverse dynamics in the development of controllers with state observers that can predict the vehicle's future motion based on current states (Schwab and Meijaard, 2013, pp. 1059-1090).

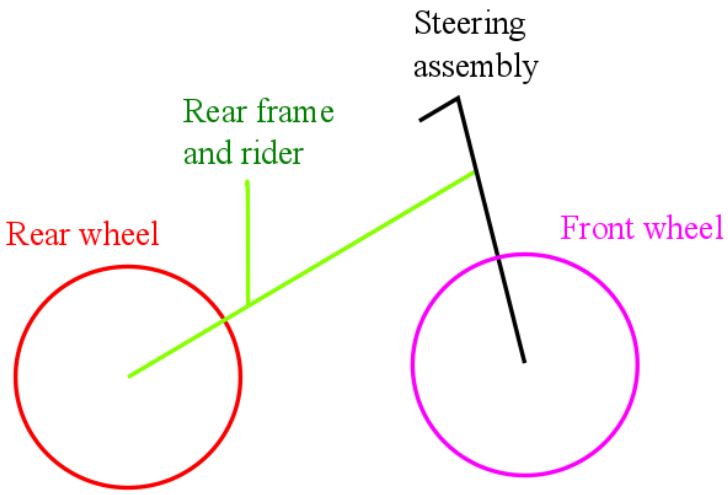

Figure 7. Bodies in the Whipple bicycle model (Schwab et al., 2012, p. 1974).

1.3 Motivation

Since their conception, vehicle handling and stability systems like ESC have been expected to reduce a high percentage of road accidents. Real-life crash report data collected since their commercialization have outdone these expectations. Aga and Okada (2003, p. 7) observed the reduction of the rate of accidents in vehicles equipped with VSC by 35% for accidents involving single cars and by 30% for automobiles having head-on collisions in Japan. Dang (2004, p. 4) analyzed crash data from five states in the USA (United States of America) to evaluate the reduction caused by ESC in crashes involving single vehicle passenger cars as

35%, crashes involving single vehicle SUVs (Sports Utility Vehicle) as 67%, fatal crashes involving single vehicle passenger cars as 30% and fatal crashes involving single vehicle SUVs as 63%. Crash data of various car models equipped with ESC in Sweden was studied by Lie et al. (2004, pp. 37-41) who estimated the effectiveness of the ESC between 20% and 40% and again by Lie et al. (2006, pp. 38-43) re-estimating the range as 13% to 35%. Both studies emphasize the positive effects of the ESC on icy road surfaces.

Data recorded by the National Highway Traffic Safety Administration shows an increase of 5.6% in the number of fatalities resulting from vehicle crashes in the USA from the year 2015 to 2016 (National Highway Traffic Safety Administration, 2018, pp. 1-11). This is lower than the 7.2% increase of crashes from 2014 to 2015 (National Highway Traffic Safety Administration, 2016, pp. 1-11). So even though the number of accidents each year is increasing still, vehicle handling systems play a key role in reducing the percentage increase. The faster we improve these systems, the closer we get to actually decreasing the accident rate per year. This indicates the pressing need to develop enhanced tire-force estimation models that can help driver assistance systems in creating a safer road traffic environment.

1.4 Objectives

The objective of this study is to create a multibody model of a bicycle which for accurate estimation of tire-road forces using a minimal set of sensors. The objective also includes validation of this multibody bicycle model using an experimental bicycle equipped with sensors measuring the actual tire-road forces.

The evident success of vehicle handling system is attributed to highly effective control algorithms and good quality data collection from sensors. Advancements in current stability systems can be achieved by making modifications in the control algorithms, building accurate dynamic models and by designing an observer that can reduce measurement errors to the maximum extent possible. This research work focuses on the second, that is, building an accurate dynamic model which can estimate tire-road forces of a vehicle on its own.

1.5 Research questions

Accuracy of tire-force estimations given by the multibody bicycle model will depend on how realistically the model is able to simulate the motion of the bicycle. As seen in the literature

review, many efforts have been put into improving the mathematical modeling of the bicycle dynamics so that a real human rider driving the bicycle can be mimicked. The method of designing the multibody system used in this research work involves the steps of coordinate selection, constraint modeling, kinematic analysis and finally the derivation of the equations of motion using inverse dynamic analysis. The solution of equations of motion can be obtained using different methods. Intricacies in each of these steps fine-tune the model towards a more realistic simulation of the system.

Therefore, to ensure that the model proposed by this research fulfills the objectives, the following research questions should be answered:

- What are the constraints that define the system?
- What is the number of degrees of freedom of the system?
- Why should inverse dynamics be used to derive the equations of motion of the bicycle?
- What is the physical interpretation of the Lagrange multipliers?

Answers to these questions will help the step by step formulation of a multibody bicycle model that can generate accurate estimations of the tire-road forces. This brings forward the main research question: Does the proposed bicycle model provide a starting point for four-wheel vehicle tire-force estimators that could be feasible for application in commercialized vehicle handling systems?

1.6 Scope

The ultimate application of this research work is in vehicle handling systems used in four wheeled vehicles. However, the scope of this study only includes the development of a multibody bicycle model. Recent works reflect the common reduction of four wheeled vehicle models to the bicycle model for simplicity. The model devised in this study should serve as a starting point for a holistic four wheel vehicle tire-force estimator that may include an observer for error reduction. So the simulation of a realistic bicycle that can move in all directions, steer and lean as a rider may choose to sufficiently defines the scope.

Also included in the scope is the subsequent validation of the model by comparing estimated values of tire-road forces with actual forces experienced by the experimental bike setup.

2 BICYCLE MULTIBODY MODELING AND EXPERIMENTATION METHODS

A step by step approach should always be taken while creating a multibody model. Figure 8 shows the detailed steps taken in this research to model the bicycle. First the equations of motions are to be derived with the steps of coordinate selection, constraint definition, kinematic analysis and dynamic analysis. A numerical example of a three-dimensional disk rolling-without-slipping is to be solved first to ensure proper understanding of the holonomic and non-holonomic constraints related to rolling-without-slipping. Forward dynamics is to be applied to the rolling disk but the bicycle model requires inverse dynamics. The experimental bicycle is to be driven to obtain experimental data needed for inverse dynamics. Solution of the equations of motion would yield Lagrange multipliers which are to be carefully interpreted to identify the reaction force estimations. The experiment would also record the actual tire-force measurements which are to be compared with the reaction force estimations in order to validate the multibody model.

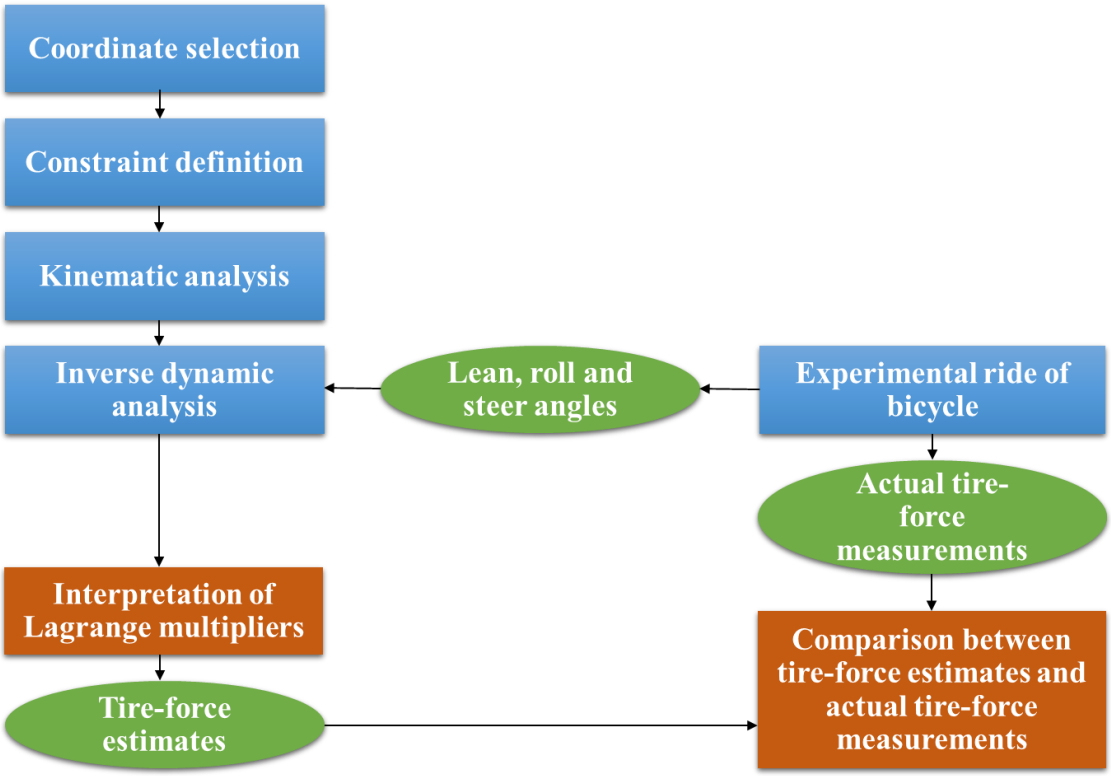

Figure 8. Method used in this research work to model the bicycle.

2.1 Numerical Example: Three-dimensional disk rolling-without-slipping

The system (Figure 9) consists of a thin disk which can roll over a smooth three-dimensional surface. It is a rigid body of infinitesimally thin cross-section of mass m_{disk}, radius r_{disk} with gravitational force g acting in downward direction. It is rolling in the $\langle XY \rangle$ global plane.

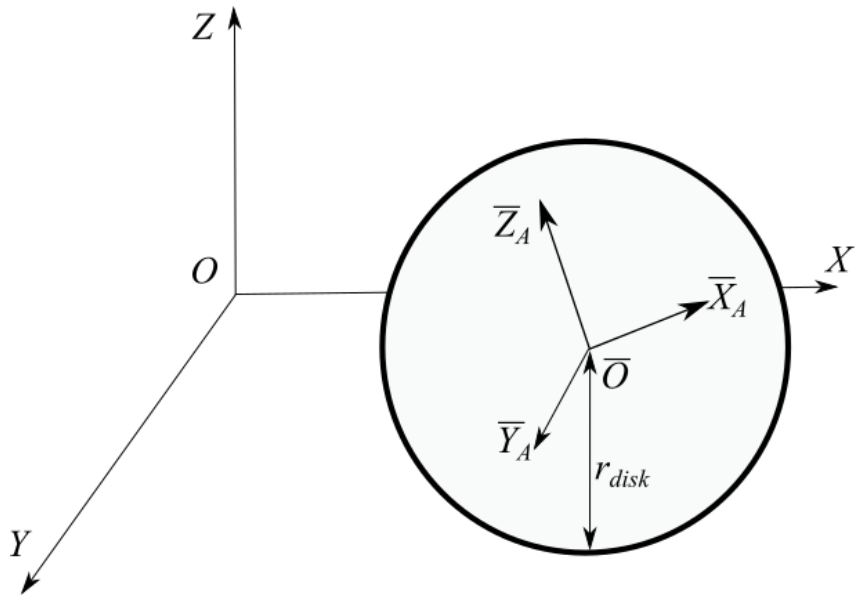

Figure 9. Three-dimensional disk rolling-without-slipping system and the coordinate systems selected.

All positions and orientations have been described with reference to the global coordinate frame $\langle X\ Y\ Z \rangle$. $\langle \bar{X}_A\ \bar{Y}_A\ \bar{Z}_A \rangle$ is the body frame of reference located at the disk's center of mass with $\bar{Z}_A$ axis normal to the surface of the disk. The origin of $\langle \bar{X}_A\ \bar{Y}_A\ \bar{Z}_A \rangle$ is located at position $\boldsymbol{R}_{A_{disk}}$ in the global frame and $\boldsymbol{A}_{disk}$ is its rotation matrix. The coordinates together form the vector $\boldsymbol{q}_{disk}$ (Shabana, 2013, pp. 85-156):

$$\boldsymbol{q}_{disk} = [R_{A_{Xdisk}} \quad R_{A_{Ydisk}} \quad R_{A_{Zdisk}} \quad \phi_{disk} \quad \theta_{disk} \quad \psi_{disk}]^T \tag{1}$$

where $R_{A_{Xdisk}}$, $R_{A_{Ydisk}}$ and $R_{A_{Zdisk}}$ describe the Cartesian coordinates of the disk's center of mass, ϕ_{disk} is the angle of rotation of the disk's body frame about the *X*-axis, θ_{disk} is the angle of rotation of the disk's body frame about the *Y*-axis, and ψ_{disk} is the angle of rotation of the disk's body frame about the *Y*-axis.

The coordinates must satisfy a set of kinematic constraints. This system is subjected to three types of constraints – the contact constraint, which ensures that the disk always has a contact point with the ground, the rolling-without-slipping constraints, which ensure that the disk rolls without slipping, and the mobility constraint which ensures the forward motion of the disk.

The position of any random point on the disk can be described in the body frame as (Shabana, 2013, pp. 85-156):

$$\overline{\boldsymbol{U}}_{pdisk} = [\quad r_{disk}\cos(\psi_{disk}) \quad 0 \quad -r_{disk}\sin(\psi_{disk})\ ]^T \tag{2}$$

The global position of this point is given by (Shabana, 2013, pp. 85-156):

$$\boldsymbol{r}_{pdisk} = \boldsymbol{q}_{disk} + \boldsymbol{A}_{disk}\overline{\boldsymbol{U}}_{pdisk} \tag{3}$$

For the point *N* (Figure 10) to maintain constant contact with the ground a holonomic contact constraint is required given by:

$$C_{1disk}: \left[\boldsymbol{r}_{pdisk}\right]_Z = 0 \tag{4}$$

where the subscript *Z* denotes the third component of the vector.

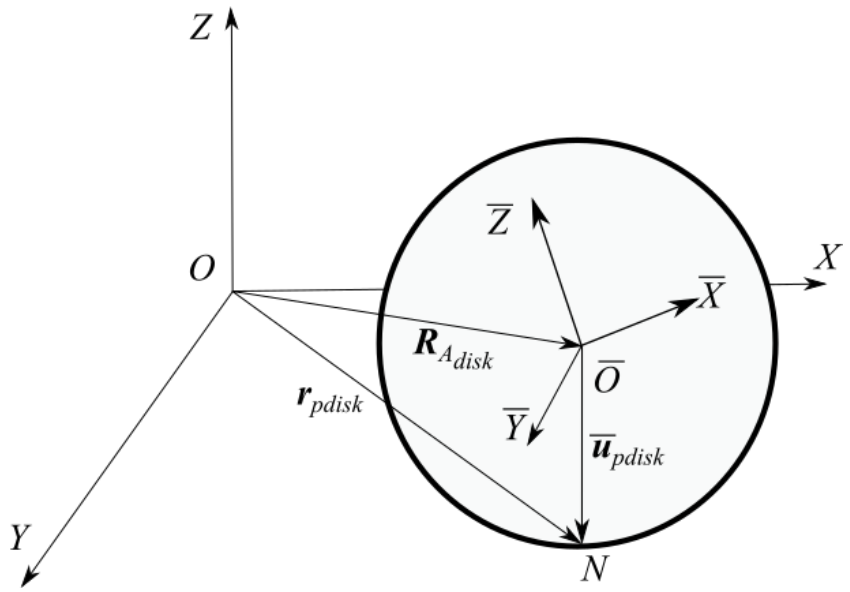

Figure 10. Position of point of contact *N* between disk and ground.

A rheonomic mobility constraint imposes the forward motion of the disk:

$$C_{2disk}: \dot{\psi}_{disk} - \frac{V_{disk}}{r_{disk}} t = 0 \tag{5}$$

where *t* is time and V_{disk} is the forward velocity of the disk.

The rolling-without-slipping constraints are the non-holonomic constraints that guarantee that distance covered by point *N* (Figure 10) while rolling must be equal to the distance covered by center of mass which is the condition of no slip. This constraint applies to velocities in both *X* and *Y* direction for which the constraints can be described as:

$$C_{nh1disk}: \dot{R}_{A_{Xdisk}} - r_{disk}\dot{\psi}_{disk}\cos(\phi_{disk}) = 0 \tag{6}$$

$$C_{nh2disk}: \dot{R}_{A_{Ydisk}} - r_{disk}\dot{\psi}_{disk}\sin(\phi_{disk}) = 0 \tag{7}$$

Therefore, for the disk the holonomic constraints vector $\boldsymbol{C}_{disk}$ and the non-holonomic constraints vector $\boldsymbol{C}_{nhdisk}$ are as follows:

$$\boldsymbol{C}_{disk} = \begin{bmatrix} R_{AZdisk} - \frac{r_{disk}\sin(\theta_{disk})}{2} - \frac{r_{disk}\sin(2\psi_{disk}+\theta_{disk})}{2} \\ \dot{\psi}_{disk} - \frac{v_{disk}}{r_{disk}} t \end{bmatrix} = 0 \tag{8}$$

$$\boldsymbol{C}_{nhdisk} = \begin{bmatrix} \dot{R}_{AXdisk} - r_{disk}\dot{\psi}_{disk}\cos(\phi_{disk}) \\ \dot{R}_{AYdisk} - r_{disk}\dot{\psi}_{disk}\sin(\phi_{disk}) \end{bmatrix} = 0 \tag{9}$$

Six coordinates in vector $\boldsymbol{q}_{disk}$ describe the disk. Since there are two non-holonomic and two holonomic constraints the disk now has two degrees of freedom. The Jacobian matrix is obtained as:

$$\boldsymbol{C}_{\boldsymbol{q}disk} = \frac{\partial \boldsymbol{C}_{disk}}{\partial \boldsymbol{q}_{disk}} =$$

$$\begin{bmatrix} 0 & 0 & 0 & 0 & 1 & 0 \\ 0 & 0 & 1 & 0 & r_{disk}\cos(2\psi_{disk}+\theta_{disk}) & -\frac{r_{disk}\cos(\theta_{disk})}{2} - \frac{r_{disk}\cos(2\psi_{disk}+\theta_{disk})}{2} \end{bmatrix} = 0 \tag{10}$$

Baumgarte stabilization factors α_B and β_B were in the derivation of the equations of motion as Lagrange equations of the first kind (Goldstein, 2011, pp. 16-22) as follows:

$$\begin{bmatrix} \boldsymbol{M}_{disk} & \boldsymbol{C}_{\boldsymbol{q}disk}^T \\ \boldsymbol{C}_{\boldsymbol{q}disk} & 0 \end{bmatrix} \begin{bmatrix} \ddot{\boldsymbol{q}}_{disk} \\ \boldsymbol{\lambda}_{disk} \end{bmatrix} = \begin{bmatrix} \boldsymbol{Q}_{edisk} + \boldsymbol{Q}_{vdisk} \\ \boldsymbol{Q}_{cdisk} \end{bmatrix} \tag{11}$$

where $\boldsymbol{M}_{disk}$ is the mass matrix of the disk, $\boldsymbol{\lambda}_{disk}$ is the Lagrange multiplier for the disk, $\boldsymbol{Q}_{cdisk}$ is the product of the Jacobian matrix and accelerations of the disk, $\boldsymbol{Q}_{edisk}$ is the vector of generalized externally applied forces and $\boldsymbol{Q}_{vdisk}$ is the quadratic velocity vector. The disk was simulated in MATLAB by introducing an initial velocity and a steering angle to check if the realistic behavior of a single wheel pushed to roll on a flat surface is simulated.

2.2 Multibody model of the bicycle

Escalona and Recuero (2012, pp. 383-402) designed a teaching course for multibody dynamics using a bicycle model simulation for engineering students. The Whipple bicycle multibody structure was used in which the body frame orientation and location were described by a minimal set of relative coordinates. Two holonomic constraints were used to describe the contact between the ground and the wheels. Four non-holonomic constraints described the condition of rolling-without-slipping for the wheels. The bicycle was driven

by a mobility constraint. Lagrange equations of the first kind (Goldstein, 2011, pp. 16-22) were used to derive the equations of motion as DAE (differential algebraic equations) and the system was subsequently transformed into an ODE (ordinary differential equation) system using the lean and steering angles as the independent coordinates. The model was successfully used to develop a real-time simulator used for educational purposes (Escalona and Recuero, 2012, pp. 383-402).

As a continuation of the Escalona and Recuero (2012, pp. 383-402) multibody bicycle dynamics course model Escalona et al. (2018, pp. 1-23) extended the symbolic implementation of the Whipple model to kinematic simulation and inverse dynamic simulation. Instrumentation was described for the validation of the model created by Escalona and Recuero (2012, pp. 383-402) and further, the lean angle, the steering angle and the rolling angle of the rear wheel were experimentally measured to perform inverse dynamic simulations. The experimental results validated the simulations in some respects while in other respects they did not agree (Escalona et al., 2018, pp. 1-23).

The Escalona et al. (2018, pp. 1-23) model of the bicycle was used as a basis for this research work. The developed model consists of a series of nine coordinates fulfilling a set of kinematic constraints. These coordinates include both dependent generalized and non-generalized coordinates. These coordinates and constraint equations help derive the equations of motion in the form of DAE. As the model includes holonomic constraints, Lagrange equations of the first kind (Goldstein, 2011, pp. 16-22) are used such that the reaction forces can be interpreted from the Lagrange multipliers.

2.3 Coordinate selection

The four bodies in the model are the rear wheel (body *i=2*), the rear frame and rider (body *i=3*), the steering assembly (body *i=4*) and the front wheel (body *i=5*). The mass of each body *i* is m^i. Radius of the wheels is *R.* The wheels are of infinitesimally thin cross-section and are assumed to be rolling-without-slipping (Escalona and Recuero, 2012, pp. 383-402).

The arbitrary positioning of the bicycle is shown in Figure 11. $\langle X\ Y\ Z\rangle$ is the global frame of reference. Intermediate frames $\langle x_{i1}\ y_{i1}\ z_{i1}\rangle$ and $\langle x_{i2}\ y_{i2}\ z_{i2}\rangle$ are used to define the bicycle frame. The Z axis of the global frame $\langle X\ Y\ Z\rangle$ is turned by angle ϕ to get intermediate frame

$\langle x_{i1}\ y_{i1}\ z_{i1}\rangle$. So axis x_{i1} makes angle ϕ with axis *X*. The x_{i1} axis of the first intermediate frame $\langle x_{i1}\ y_{i1}\ z_{i1}\rangle$ is turned by angle θ to get the second intermediate frame $\langle x_{i2}\ y_{i2}\ z_{i2}\rangle$ which is located at the point of contact of the rear wheel with the ground *C*. So axis z_{i2} makes angle θ with axis z_{i1}. Each body's own frame located at its respective center of mass $\boldsymbol{G}_i$ at distance $\bar{\boldsymbol{r}}_{G_i}$ from each other, is defined as $\langle x_i\ y_i\ z_i\rangle$ where *i* is the body number. The y_{i2} axis of the second intermediate frame $\langle x_{i2}\ y_{i2}\ z_{i2}\rangle$ is turned by angle ψ to get the body frame of the rear wheel $\langle x_2\ y_2\ z_2\rangle$. So axis z_2 makes angle ψ with axis z_{i2}. The y_2 axis of the rear wheel body frame $\langle x_2\ y_2\ z_2\rangle$ is turned by angle β to get the body frame of the rear frame and rider $\langle x_3\ y_3\ z_3\rangle$. So axis z_3 makes angle β with axis z_2. The z_3 axis of the rear frame and rider body frame $\langle x_3\ y_3\ z_3\rangle$ is turned by angle γ to get the body frame of the steering assembly $\langle x_4\ y_4\ z_4\rangle$. So axis x_4 makes angle γ with axis x_3. The y_4 axis of the steering assembly frame $\langle x_4\ y_4\ z_4\rangle$ is turned by angle ϵ to get the body frame of the front wheel $\langle x_5\ y_5\ z_5\rangle$. So axis x_5 makes angle ϵ with axis x_4. (Escalona and Recuero, 2012, pp. 383-402)

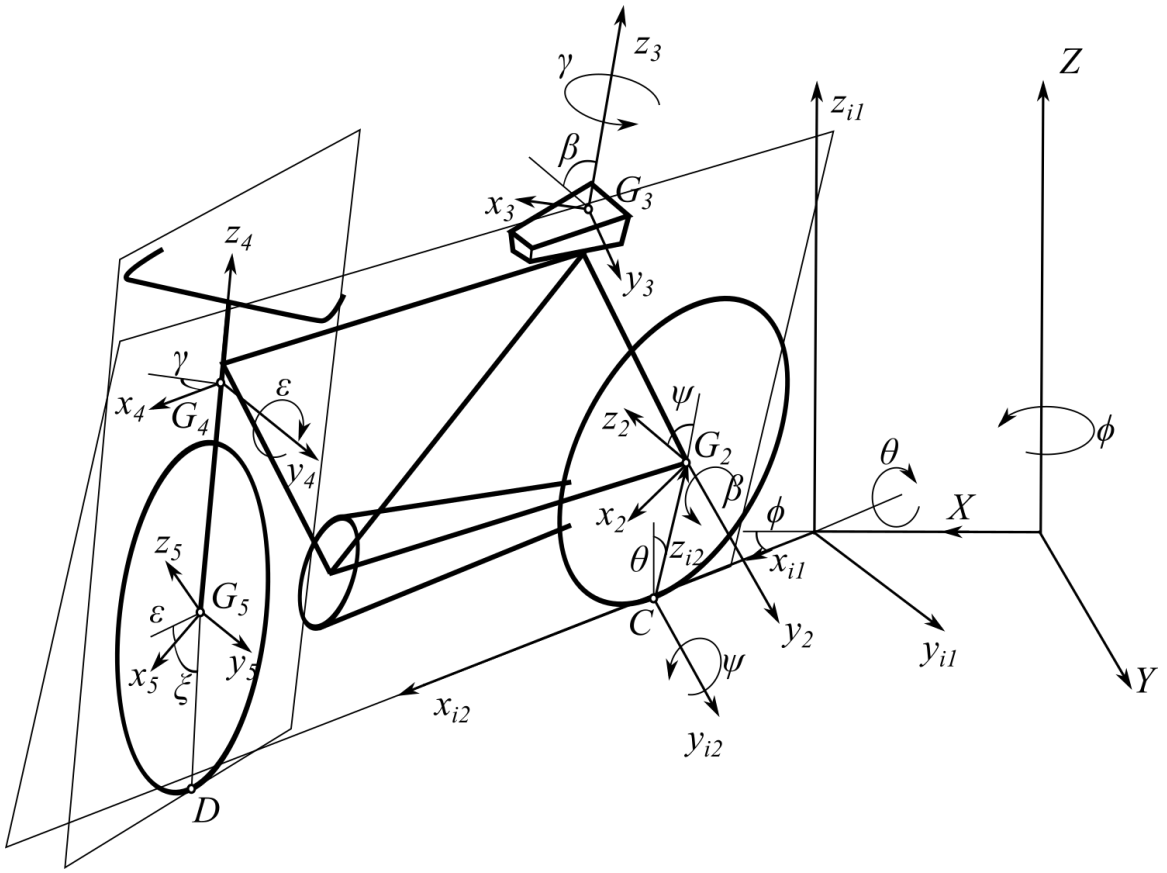

Figure 11. Description of bicycle model coordinates and frames (mod. Escalona and Recuero, 2012, p. 386).

The coordinates of the point of contact between the rear wheel and the ground and the angles by which the frames have been turned describe the global position and orientation of the bicycle. The selected coordinates are grouped together in the vector (Escalona et al., 2018, pp. 1-23):

$$\boldsymbol{q} = [x_C \quad y_C \quad \phi \quad \theta \quad \psi \quad \beta \quad \gamma \quad \epsilon \quad \xi]^T \tag{12}$$

Where ϵ is the front wheel rolling angle, γ is the steering angle, β is the rear frame pitch angle, ψ is the rear wheel rolling angle (pitch), θ is the lean (roll) angle, ϕ is the heading (yaw) angle, x_C and y_C describe the global position of point *C* in the $\langle XY \rangle$ plane and ξ is the angle made by the radius containing point *D* (contact point between the front wheel and the ground) with the *x*-axis of the front wheel body frame (x_5).

While all the other selected angles in the vector $\boldsymbol{q}$ represent rotations about the body frame axes as shown in Figure 11, ξ is not a Cartesian coordinate defined with respect to any of the reference frames. It is defined with respect to a geometric feature which is the point of contact between the ground and the front wheel *D*. This makes ξ a non-generalized parameter essential for the contact modelling of the bicycle wheels. This can be understood from the contact modelling implementation of Shabana and Sany (2001, pp. 183-204) in a multibody algorithm that can used for any general purpose. It highlights the necessity of mixed set containing both generalized and non-generalized coordinates in formulating the kinematic constraints that describe the contact between two surfaces. Only by solving this mixed set can the contact points be known during online simulation (Shabana and Sany, 2001, pp. 183-204).

The contact point *D* is unknown prior to performing positional analysis to the whole bicycle system making the parameter ξ an unknown function of time. The position of the contact point *D* can be predicted after solving the coupled set of generalized coordinates and non-generalized parameter given in vector $\boldsymbol{q}$. Therefore, the parameter ξ is a non-generalized parameter with no associated inertia forces. The geometric parameter ξ and the system's generalized coordinates will be used to formulate the contact constraints.

2.4 Constraints

The bicycle system is bound by three types of kinematic constraints - the contact constraints which ensure a contact point between the front wheel and the ground always, the rolling-without-slipping constraints which ensure that both wheels roll without slipping on the ground, and the mobility constraint that guarantees forward velocity of the bicycle to be approximately constant always.

The contact constraints are based on two conditions. First, the location of the point of contact on the wheel should be at the same spatial location as the point of contact on the ground. Second, the tangent at the point of contact of the wheel should be parallel to that at the point of contact on the ground. The coordinate selection ensures that these conditions are satisfied by the rear wheel (Escalona and Recuero, 2012, pp. 383-402). The position of any random point *P* on the front wheel is given by (Escalona and Recuero, 2012, pp. 383-402):

$$\bar{\boldsymbol{r}}^5{}_P = [\quad R\cos(\xi) \quad 0 \quad -R\sin(\xi)\ ]^T \tag{13}$$

where $\xi \in [0, 2\pi]$

The tangent vector at point *P* is given by (Escalona and Recuero, 2012, pp. 383-402):

$$\boldsymbol{t}^5{}_P = \frac{\partial \bar{\boldsymbol{r}}^5{}_P}{\partial \xi} = [\quad R\sin(\xi) \quad 0 \quad -R\cos(\xi)\ ]^T \tag{14}$$

where $\xi \in [0, 2\pi]$

Therefore, the position and tangent vectors can be obtained as (Escalona and Recuero, 2012, pp. 383-402):

$$\boldsymbol{r}_P(\xi) = \boldsymbol{r}_{G_5} + \boldsymbol{A}^5 \bar{\boldsymbol{r}}^5{}_P \tag{15}$$

$$\boldsymbol{t}_P(\xi) = \boldsymbol{A}^5 \boldsymbol{t}^5{}_P \tag{16}$$

where $\xi \in [0, 2\pi]$

As the wheel is of infinitesimally thin cross-section the contact constraints at point of contact *D* can be written as:

$$C^{con}{}_1 : [\boldsymbol{r}_D(\boldsymbol{q}, \xi)]_Z = 0 \tag{17}$$

$$C^{con}{}_2 : [\boldsymbol{t}_D(\boldsymbol{q}, \xi)]_Z = 0 \tag{18}$$

$$\boldsymbol{C}^{con}(\boldsymbol{q}) = 0 \tag{19}$$

where the subscript *Z* indicates the vectors' third components.

The contact constraints are scleronomic as there is no explicit appearance of time, and also holonomic because of no appearance of generalized velocities.

The rolling-without-slipping constraints are based on the condition that the contact-point velocity must be zero. The rear wheel velocity is given by (Escalona and Recuero, 2012, pp. 383-402):

$$\boldsymbol{v}_c = \boldsymbol{v}_{G_2} + \boldsymbol{\omega}^2 \wedge \boldsymbol{r}_{G_2C} \tag{20}$$

where $\boldsymbol{v}_c$ is the velocity of contact point *C*, $\boldsymbol{v}_{G_2}$ is the velocity of center of mass of the rear wheel G_2, $\boldsymbol{\omega}^2$ is the rear wheel angular velocity and $\boldsymbol{r}_{G_2C}$ is the position of point *C* in the body frame of the rear wheel given by (Escalona and Recuero, 2012, pp. 383-402):

$$\boldsymbol{r}_{G_2C} = \boldsymbol{A}^{i2}[0 \quad 0 \quad -R]^T \tag{21}$$

On evaluating the velocity $\boldsymbol{v}_c$ we get (Escalona and Recuero, 2012, pp. 383-402):

$$\boldsymbol{v}_c = \begin{bmatrix} \dot{x}_C - R\cos(\phi)\dot{\psi} \\ \dot{y}_C - R\sin(\phi)\dot{\psi} \\ 0 \end{bmatrix} \tag{22}$$

Therefore, for the rear wheel (body *i*= *2*) the rolling-without-slipping constraints can be obtained as:

$$C^{rws}{}_1 : \dot{x}_C - R\cos(\phi)\dot{\psi} = 0 \tag{23}$$

$$C^{rws}{}_2 : \dot{y}_C - R\sin(\phi)\dot{\psi} = 0 \tag{24}$$

$$\boldsymbol{C}^{rws,2}(\boldsymbol{q}, \dot{\boldsymbol{q}}) = 0 \tag{25}$$

Similarly, for the front wheel (body *i= 5*) the rolling-without-slipping constraints can also be obtained using velocity of point *D* $\boldsymbol{v}_D$ as:

$$C^{rws}{}_3 : [\boldsymbol{v}_D]_X = 0 \tag{26}$$

$$C^{rws}{}_4 : [\boldsymbol{v}_D]_Y = 0 \tag{27}$$

$$\boldsymbol{C}^{rws,5}(\boldsymbol{q}, \dot{\boldsymbol{q}}) = 0 \tag{28}$$

The rolling-without-slipping constraints are are non-integrable functions of $\boldsymbol{q}$ and $\dot{\boldsymbol{q}}$ so they are non-holonomic.

The Jacobian of the rolling-without-slipping constraints is (Escalona and Recuero, 2012, pp. 383-402):

$$\boldsymbol{B}^i = \frac{\partial \boldsymbol{C}^{rws,i}}{\partial \dot{\boldsymbol{q}}} \tag{29}$$

where *i=2,3,4,5*.

For the rear wheel (body *i=2*) the Jacobian of the rolling-without-slipping constraints can be evaluated as (Escalona and Recuero, 2012, pp. 383-402):

$$\boldsymbol{B}^2 = \begin{bmatrix} 1 & 0 & 0 & 0 & -R\cos(\phi) & 0 & 0 & 0 & 0 \\ 0 & 1 & 0 & 0 & -R\sin(\phi) & 0 & 0 & 0 & 0 \end{bmatrix} \tag{30}$$

Now, the bicycle model is described using nine selected coordinates and subjected to six constraints. Therefore, the system has *9-6=3* degrees of freedom.

The direct or forward dynamic analysis, without the use of experimental data, can now be performed using these constraints. But for the bicycle to be moving forward in this direct

dynamic simulation there needs to be a constraint that drives the bicycle forward. To establish this driving forward of the bicycle a mobility constraint containing forward velocity *V* has been imposed on the bicycle. This constraint can be written as (Escalona and Recuero, 2012, pp. 383-402):

$$\dot{\psi} - \frac{V}{R}t = 0 \tag{31}$$

$$\boldsymbol{C}^{mob}(q,t) = 0 \tag{32}$$

The mobility constraint is a rheonomic constraint because of explicit appearance of time. Later, when the dynamic coordinates driving the bicycle are experimentally obtained this constraint will be modified accordingly.

The total set of constraints can be expressed as (Escalona and Recuero, 2012, pp. 383-402):

$$\boldsymbol{C}(\boldsymbol{q},\dot{\boldsymbol{q}},t) = \begin{bmatrix} \boldsymbol{C}^{con}(\boldsymbol{q}) \\ \boldsymbol{C}^{rws}(\boldsymbol{q},\dot{\boldsymbol{q}}) \\ \boldsymbol{C}^{mob}(\boldsymbol{q},t) \end{bmatrix} \tag{33}$$

2.5 Kinematics

Based on the selected coordinates, each body frame's position and orientation are obtained in the global frame as (Escalona et al., 2018, pp. 1-23):

$$\boldsymbol{R}^i = \boldsymbol{R}^i(\boldsymbol{q}) \tag{34}$$

$$\boldsymbol{A}^i = \boldsymbol{A}^i(\boldsymbol{q}) \tag{35}$$

where *i=2,3,4,5*.

The position of the center of gravity of the rear wheel (body *i=2*) is (Escalona and Recuero, 2012, pp. 383-402):

$$\boldsymbol{R}^2_{G_2} = \boldsymbol{r}_C + \boldsymbol{A}^{i2}\bar{\boldsymbol{r}}^{i2}_{G_2} = \begin{bmatrix} x_C \\ y_C \\ 0 \end{bmatrix} + \begin{bmatrix} \sin(\phi)\sin(\theta) \\ -\cos(\phi)\sin(\theta) \\ \cos(\theta) \end{bmatrix} R \tag{36}$$

The Jacobian matrices are symbolically computed as (Escalona et al., 2018, pp. 1-23):

$$\boldsymbol{H}^i = \frac{\partial \boldsymbol{R}^i}{\partial \boldsymbol{q}} \tag{37}$$

$$\bar{\boldsymbol{G}}^i = \frac{\partial \bar{\boldsymbol{\omega}}^i}{\partial \dot{\boldsymbol{q}}} \tag{38}$$

where $\bar{\boldsymbol{\omega}}$ is the angular velocity vector and *i=2, 3, 4, 5*.

Jacobian matrix of the rear wheel's (body *i=2*) center of gravity's position $\boldsymbol{R}_{G_2}^2$ with respect to $\boldsymbol{q}$ is given by (Escalona and Recuero, 2012, pp. 383-402):

$$\boldsymbol{H}^2 = \begin{bmatrix} 1 & 0 & R\cos(\phi)\sin(\theta) & R\sin(\phi)\cos(\theta) & 0 & 0 & 0 & 0 & 0 \\ 0 & 1 & R\sin(\phi)\sin(\theta) & -R\cos(\phi)\cos(\theta) & 0 & 0 & 0 & 0 & 0 \\ 0 & 0 & 0 & -R\sin(\theta) & 0 & 0 & 0 & 0 & 0 \end{bmatrix} \tag{39}$$

Jacobian matrix of the orientation of the rear wheel (body *i=2*) with respect to $\boldsymbol{q}$ is given by (Escalona and Recuero, 2012, pp. 383-402):

$$\bar{\boldsymbol{G}}^2 = \begin{bmatrix} 0 & 0 & -\cos(\theta)\sin(\psi) & \sin(\psi) & 0 & 0 & 0 & 0 & 0 \\ 0 & 0 & \sin(\theta) & 0 & 1 & 0 & 0 & 0 & 0 \\ 0 & 0 & \cos(\theta)\sin(\psi) & \sin(\psi) & 0 & 0 & 0 & 0 & 0 \end{bmatrix} \tag{40}$$

The absolute velocity and angular velocity vectors are found as (Escalona et al., 2018, pp. 1-23):

$$\boldsymbol{v}_G^i = \boldsymbol{H}^i(\boldsymbol{q})\dot{\boldsymbol{q}} \tag{41}$$

$$\bar{\boldsymbol{\omega}}_G^i = \bar{\boldsymbol{G}}^i(\boldsymbol{q})\dot{\boldsymbol{q}} \tag{42}$$

where *i=2, 3, 4, 5*.

The velocity of the rear wheel's (body *i=2*) center of gravity is given by the time derivative of (36) (Escalona and Recuero, 2012, pp. 383-402):

$$\boldsymbol{v}_G^2 = \boldsymbol{H}^2(\boldsymbol{q})\dot{\boldsymbol{q}} = \begin{bmatrix} \dot{x}_C \\ \dot{y}_C \\ 0 \end{bmatrix} + \begin{bmatrix} \cos(\phi)\sin(\theta)\,\dot{\phi} + \sin(\phi)\cos(\theta)\,\dot{\theta} \\ \sin(\phi)\sin(\theta)\,\dot{\phi} - \cos(\phi)\cos(\theta)\,\dot{\theta} \\ -\sin(\theta)\,\dot{\theta} \end{bmatrix} R \tag{43}$$

The Jacobian matrices obtained from these are (Escalona et al., 2018, pp. 1-23):

$$\boldsymbol{h}^i = \frac{\partial \boldsymbol{v}_G^i}{\partial \boldsymbol{q}} \tag{44}$$

$$\overline{\boldsymbol{g}}^i = \frac{\partial \overline{\boldsymbol{\omega}}^i}{\partial \boldsymbol{q}} \tag{45}$$

where *i=2, 3, 4, 5.*

The accelerations are found similarly as (Escalona et al., 2018, pp. 1-23):

$$\boldsymbol{a}_G^i = \boldsymbol{H}^i(\boldsymbol{q})\ddot{\boldsymbol{q}} + \boldsymbol{h}^i(\boldsymbol{q})\dot{\boldsymbol{q}} \tag{46}$$

$$\overline{\boldsymbol{\alpha}}^i = \overline{\boldsymbol{G}}^i(\boldsymbol{q})\ddot{\boldsymbol{q}} + \overline{\boldsymbol{g}}^i(\boldsymbol{q})\dot{\boldsymbol{q}} \tag{47}$$

where *i=2, 3, 4, 5.*

2.6 Dynamics

For deriving the bicycle's equations of motion first its kinetic energy, the vector of generalized gravity forces, the vector of generalized external forces, the generalized inertia forces and the quadratic velocity vector have to be computed.

The sum of the bicycle's translational kinetic energy and rotational kinetic energy gives its total kinetic energy (Shabana, 2013, pp. 85-156):

$$T = \sum_{n=2}^{5} \frac{1}{2}\left[m^i(\boldsymbol{v}_{G_i})^T\boldsymbol{v}_{G_i} + (\overline{\boldsymbol{\omega}}^i)^T\overline{\boldsymbol{I}}^i\overline{\boldsymbol{\omega}}^i\right] \tag{48}$$

where m^i is the mass and $\bar{I}^i$ is the inertia of each body. Substituting v_{G_i} and $\bar{\omega}^i$ from (41) and (42) we obtain the kinetic energy in compact form as (Escalona and Recuero, 2012, pp. 383-402):

$$T = \frac{1}{2}\dot{\boldsymbol{q}}^T \boldsymbol{M} \dot{\boldsymbol{q}} \tag{49}$$

where *M* is the mass matrix given by (Escalona and Recuero, 2012, pp. 383-402):

$$\boldsymbol{M} = \sum_{n=2}^{5} \left[m^i \boldsymbol{H}^{i^T} \boldsymbol{H}^i + \overline{\boldsymbol{G}}^{i^T} \overline{\boldsymbol{I}}^i \overline{\boldsymbol{G}}^i \right] \tag{50}$$

The vector of generalized external forces can be written as (Escalona and Recuero, 2012, pp. 383-402):

$$\boldsymbol{Q}_{ext} = [F_{xC} \quad F_{yC} \quad M_\phi \quad M_\theta \quad M_\psi \quad M_\beta \quad M_\gamma \quad M_\epsilon \quad M_\xi] \tag{51}$$

where each element is the force or moment associated with a specific coordinate denoted in the subscript. Here $M_\xi = 0$ as ξ is a non-generalized coordinate which does not contribute to the velocities of the bicycle (Escalona and Recuero, 2012, pp. 383-402).

The virtual power of the gravity forces is derived to obtain the vector of generalized gravity forces. The virtual magnitude of this power is given by (Escalona and Recuero, 2012, pp. 383-402):

$$\dot{W}^*_{grav} = \sum_{n=2}^{5} \boldsymbol{P}^{i^T} \boldsymbol{v}^*_{G_i} = \left(\sum_{n=2}^{5} \boldsymbol{P}^{i^T} \boldsymbol{H}^i \right) \dot{\boldsymbol{q}} \tag{52}$$

where the superscript * indicates virtual magnitude and P^i is the weight vector of body *i* given by (Escalona and Recuero, 2012, pp. 383-402):

$$\boldsymbol{P}^i = [0 \quad 0 \quad -m_i g] \tag{53}$$

Therefore, the vector of generalized gravity forces is obtained as (Escalona and Recuero, 2012, pp. 383-402):

$$\boldsymbol{Q}_{grav} = \left(\sum_{n=2}^{5} \boldsymbol{H}^{i^T} \boldsymbol{P}^i \right) \tag{54}$$

The generalized inertia forces can be obtained by (Escalona and Recuero, 2012, pp. 383-402):

$$\frac{d}{dt}\left(\frac{\partial T}{\partial \dot{\boldsymbol{q}}}\right) = \boldsymbol{M}\ddot{\boldsymbol{q}} + \dot{\boldsymbol{M}}\dot{\boldsymbol{q}} \tag{55}$$

$$\frac{\partial T}{\partial \boldsymbol{q}} = \frac{1}{2}\frac{\partial(\boldsymbol{M}\dot{\boldsymbol{q}})}{\partial \boldsymbol{q}}\dot{\boldsymbol{q}} \tag{56}$$

The inertia forces comprise of forces quadratic with respect to the system velocities and those that are proportional to the system accelerations. This quadratic velocity vector is expressed as (Escalona and Recuero, 2012, pp. 383-402):

$$\boldsymbol{Q}_v = -\dot{\boldsymbol{M}}\dot{\boldsymbol{q}} + \frac{1}{2}\frac{\partial(\boldsymbol{M}\dot{\boldsymbol{q}})}{\partial \boldsymbol{q}}\dot{\boldsymbol{q}} \tag{57}$$

The bicycle's equations of motion are derived in the form of Lagrange equations of the first kind (Goldstein, 2011, pp. 16-22) as (Escalona and Recuero, 2012, pp. 383-402):

$$\frac{d}{dt}\left(\frac{\partial T}{\partial \dot{\boldsymbol{q}}}\right) - \frac{\partial T}{\partial \boldsymbol{q}} + \boldsymbol{D}_h{}^T\boldsymbol{\lambda} = \boldsymbol{Q}_v + \boldsymbol{Q}_{grav} + \boldsymbol{Q}_{ext} \tag{58}$$

where $\boldsymbol{D}_h$ is the Jacobian of the holonomic constraints and $\boldsymbol{\lambda}$ is the vector of Lagrange multipliers.

When the vectors are substituted in the above equation, the equations of motion becomes (Escalona and Recuero, 2012, pp. 383-402):

$$\boldsymbol{M}\ddot{\boldsymbol{q}} + \boldsymbol{D}_h{}^T\boldsymbol{\lambda} = \boldsymbol{Q}_v + \boldsymbol{Q}_{grav} + \boldsymbol{Q}_{ext} \tag{59}$$

2.7 Reaction forces

The second term in the equation of motion indicates the vector of generalized reaction forces $\boldsymbol{Q}_{reac}$ which appears in the system because of the constraints. The Lagrange multipliers are used to calculate this vector and to indicate the reaction forces while the Jacobian of all the

constraints indicates the location and orientation of all the reaction forces. The Jacobian of all the constraints is given by (Escalona and Recuero, 2012, pp. 383-402):

$$\boldsymbol{D}_h = \begin{bmatrix} \boldsymbol{C}_{\boldsymbol{q}}^{con} \\ \boldsymbol{C}_{\boldsymbol{q}}^{rws} \\ \boldsymbol{C}_{\boldsymbol{q}}^{mob} \end{bmatrix} \tag{60}$$

Using the Jacobian matrix $\boldsymbol{D}_h$ and the Lagrange multipliers, the vector of generalized reaction forces can be evaluated as (Escalona and Recuero, 2012, pp. 383-402):

$$\boldsymbol{Q}_{reac} = -\boldsymbol{D}_h{}^T \boldsymbol{\lambda} \tag{61}$$

2.8 Experimental setup

The model is validated by a bicycle equipped with sensors to gather data that was used by Escalona et al. (2018, pp. 1-23). The sensors are used to track the actions taken by the cyclist and measure the actual tire-road forces. Therefore, the main objectives of the experiments are to gather sensor data for inverse dynamic analysis and to validate the obtained reaction forces experimentally. The experimental setup is shown in Figure 12.

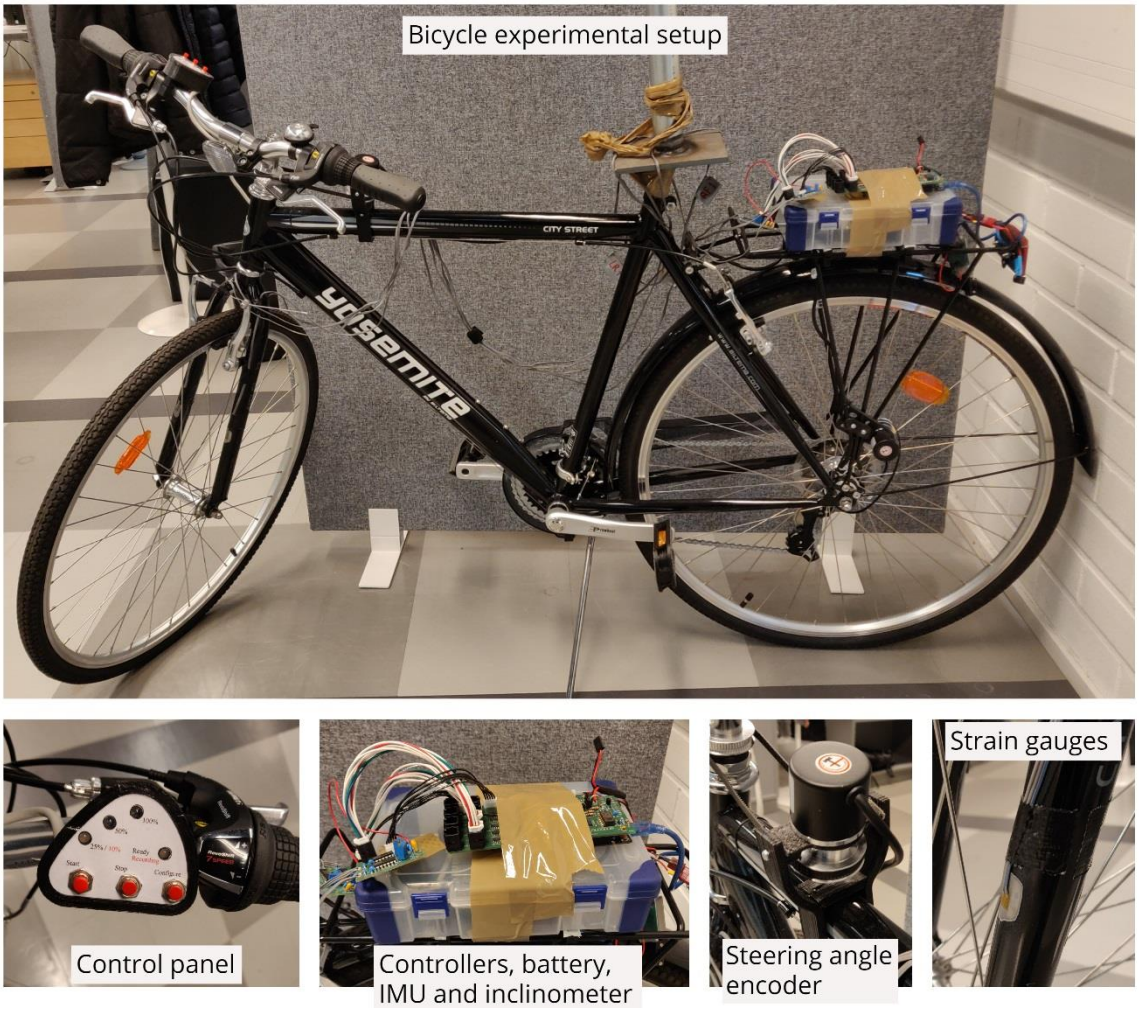

Figure 12. Bicycle experimental setup.

The coordinates that need to be measured from the experiment are the steering angle γ, the rear frame rolling angle ψ and the lean angle θ, which together form the dynamic coordinates of the system. To measure these angles during the bike ride data-acquisition system consisting of an Arduino Due board, a Raspberry Pi 3 computer and some sensors has been installed in the bicycle. Communication between the data-acquisition system and the user or "client" is through Wi-Fi. The data is then processed by the "client" and a visualization of the bicycle motion is created on a laptop or smartphone. The setup also includes an IMU (Inertial Measurement Unit). It consisting of a three axis digital accelerometer and gyroscope to measure the acceleration and angular velocity of the rear frame. The specifications of all the sensors are given below in Table 1. (Escalona et al., 2018, pp. 1-23.)

Table 1. Sensor specifications (Escalona et al., 2018, pp. 13).

Sensor	Model Name	Range	Measures
IMU	BMI160	- Selectable angular velocity range ±125, ±250, ±500, ±1000, ±2000°/s - Selectable accelerations range ±2, ±4, ±8, ±16 g	Accelerations and angular velocity
Inclinometer	G-NSDOG2-001	Range ±20°	Lean angle θ
Encoders	LPD3806-600BM-G5-24G	2400 pulses/rev	Rolling angle ψ and steering angle γ

The rolling angle is measured by the rotary encoder in the rear wheel and the steering angle is measured by the one in the steering assembly. This results in the measured rolling angle ψ being affected by the rear frame pitch angle β. However, as ψ is a large angle and β is changing slightly, the measured angle ψ is considered to be a good estimate. (Escalona et al., 2018, pp. 1-23.)

The Arduino board is connected to all the sensors. The Raspberry Pi 3 is required for data sampling critical to time and communication with smart phone or laptops through Wi-Fi. The other quantities to be measured from the experiments are the actual tire-road forces. For the force measurements, the bike has been equipped with four strain gauges on the front wheel fork to measure these forces. (Escalona et al., 2018, pp. 1-23.)

2.9 Inverse dynamic analysis

From the experiments, the steering angle, the lean angle and the rolling angle of the rear wheel at every time step are recorded as the cyclist rides the bike. These angles are the dynamic coordinates obtained from the experiment which describe the cyclists actions. Earlier, for the forward dynamics the mobility constraint had been defined by imposing an approximately constant forward velocity on the bicycle. With the help of the experimental data the mobility constraint can now be redefined to take into account the cyclist's actions and create an inverse dynamic simulation mimicking the exact movements in the experiment. The mobility constraint can now be rewritten as (Escalona et al., 2018, pp. 1-23):

$$\boldsymbol{C}^{mob}(\boldsymbol{q},t)=\begin{bmatrix}\theta\\ \psi\\ \gamma\end{bmatrix}-\begin{bmatrix}\theta^{exp}\\ \psi^{exp}\\ \gamma^{exp}\end{bmatrix}=0 \tag{62}$$

where $\theta^{exp}$is the experimental lean angle, ψ^{exp} is the experimental rolling angle of the rear wheel and γ^{exp} is the experimental steering angle.

Nine coordinates now described the bicycle which is subjected to nine constraints (two holonomic constraints, four non-holonomic constraints and three mobility constraints). This gives the system *9-9=0* degrees of freedom. The simulation model's time step must match the sampling period of the sensors. As the mobility constraint is time dependent, its time derivative can be augmented with the Jacobian of the other constraints as (Escalona et al., 2018, pp. 1-23):

$$\begin{bmatrix}\boldsymbol{C}_{\boldsymbol{q}}^{con}\\ \boldsymbol{C}_{\boldsymbol{q}}^{rws}\\ \boldsymbol{C}_{\boldsymbol{q}}^{mob}\end{bmatrix}\dot{\boldsymbol{q}}+\begin{bmatrix}0\\ 0\\ \boldsymbol{C}_{t}^{mob}\end{bmatrix}=\boldsymbol{D}_h\dot{\boldsymbol{q}}+\boldsymbol{E}=0 \tag{63}$$

where $\boldsymbol{D}_h$ is the coordinate-dependent term, $\boldsymbol{E}$ is the time dependent term and the time derivative of the mobility constraint is given by (Escalona et al., 2018, pp. 1-23):

$$\boldsymbol{C}_{t}^{mob}=\begin{bmatrix}\dot{\theta}^{exp}\\ \dot{\psi}^{exp}\\ \dot{\gamma}^{exp}\end{bmatrix} \tag{64}$$

The equation of motion (59) can now be written as (Escalona et al., 2018, pp. 1-23):

$$\begin{bmatrix}\boldsymbol{M} & \boldsymbol{D}_h{}^{T}\\ \boldsymbol{D}_h & 0\end{bmatrix}\begin{bmatrix}\ddot{\boldsymbol{q}}\\ \boldsymbol{\lambda}\end{bmatrix}=\begin{bmatrix}\boldsymbol{Q}_v+\boldsymbol{Q}_{grav}+\boldsymbol{Q}_{ext}\\ -\dot{\boldsymbol{D}_h}\dot{\boldsymbol{q}}-\dot{\boldsymbol{E}}\end{bmatrix} \tag{65}$$

2.10 Understanding the Lagrange multipliers

On solving the equation of motion (65) using MATLAB the vector Lagrange multipliers can be obtained. The first Lagrange multiplier λ_1 is associated with the first contact constraint.

its physical interpretation is the normal contact force acting on the front wheel in opposite direction. There are no Lagrange multipliers for the rear wheel normal forces as there are no constraints associated with it (Escalona et al., 2018, pp. 1-23). The second Lagrange multiplier is always zero as it is associated to the tangential displacement of the front wheel (Schwab, 2014, pp. 22-27). Lagrange multipliers λ_3, λ_4, λ_5 and λ_6 are related to the non-holonomic rolling-without-slipping constraints. They indicate the components of the lateral and longitudinal contact forces acting on the wheels. Lagrange multipliers λ_7, λ_8 and λ_9 associated with the mobility constraints can be interpreted as the generalized forces required to drive the respective movements in opposite direction (Escalona et al., 2018, pp. 1-23). The contact forces can now be compared to the actual forces obtained from strain gauges in the experimental measurements to validate them. (Escalona et al., 2018, pp. 1-23.)

3 SIMULATION RESULTS AND ANALYSIS

The complete modeling method explained in the previous chapter was implemented in MATLAB to simulate the bicycle and obtain the Lagrange multipliers. Before that the numerical example of the simple rolling disk problem was tried out using the same method. The rolling disk was simulated using forward dynamics. But for the bicycle simulation the experimental bike was driven to obtain the variables required for inverse dynamic simulation and thereafter, the Lagrange multipliers were interpreted as the associated forces.

3.1 Simulation of disk rolling-without-slipping

The single-disk system was simulated by using the derived equations of motion as shown in Figure 13 with the parameters given in Table 2.

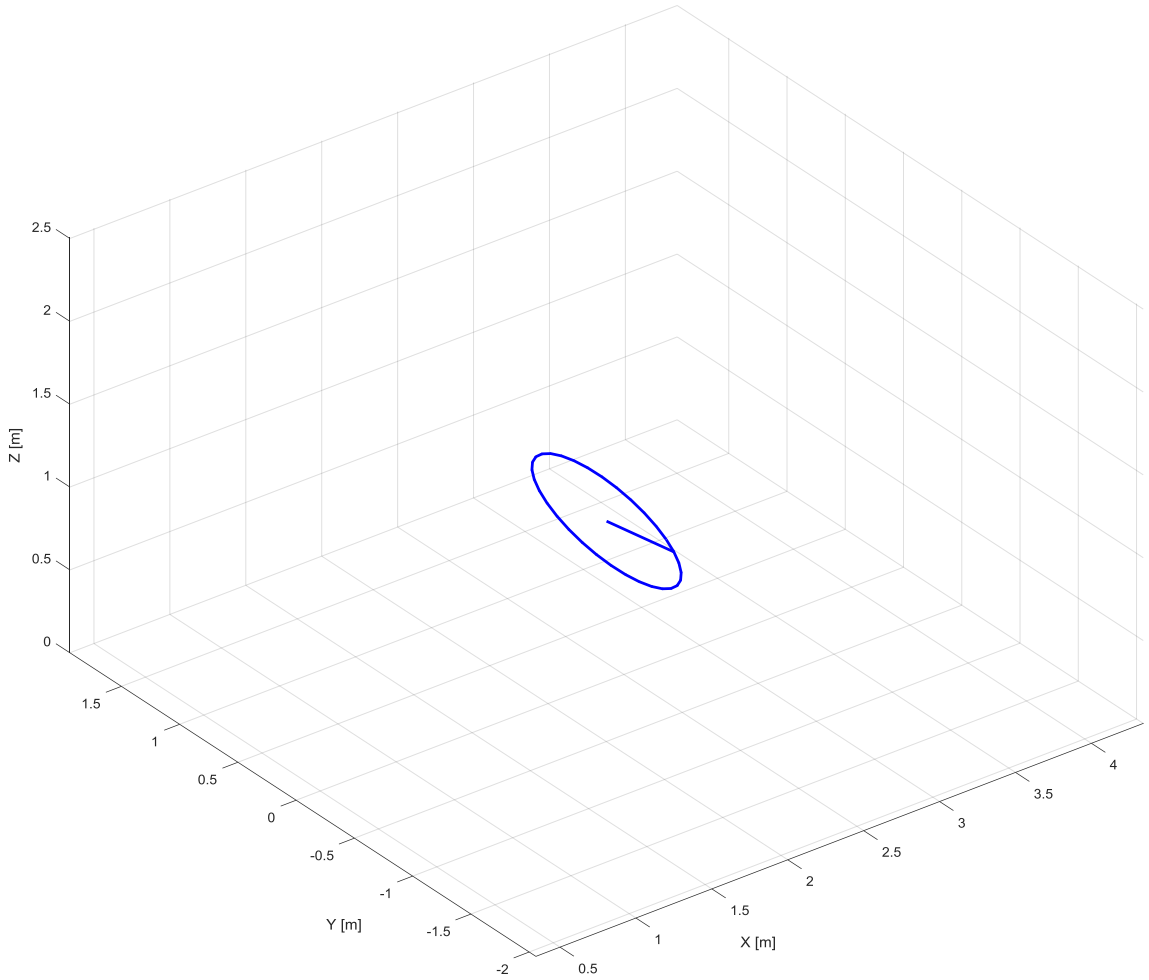

Figure 13. Simulation of rolling disk.

Table 2. Rolling disk simulation parameters.

Radius of disk, r	0.5 m
Mass of disk, m	10 kg
Acceleration due to gravity, g	9.81 m/s^2
Forward velocity, V	20 m/s
Baumgarte stabilization factor, α_B	1
Baumgarte stabilization factor, β_B	1

The trajectory of the disk when plotted for a span of 5 seconds is shown in Figure 14.

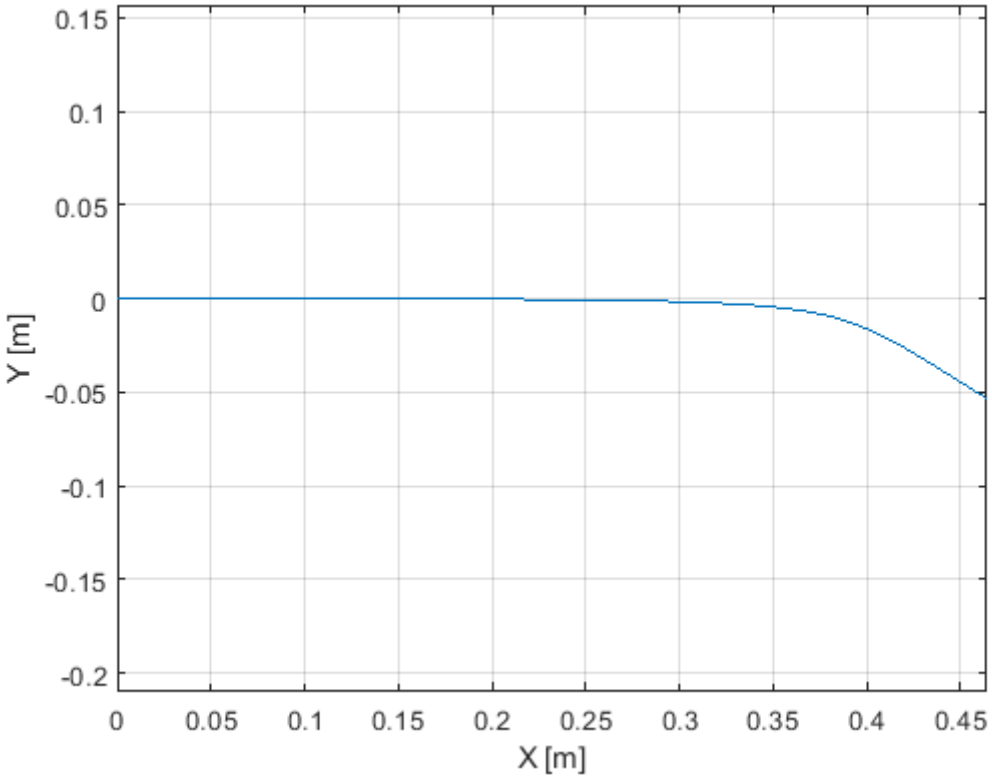

Figure 14. Trajectory of rolling disk.

The disk is seen to be rolling in the simulation on the $\langle XY \rangle$ plane according to the given variables. The disk rolls forward, steers slightly left and eventually falls face flat on the ground. The results give an accurate description of the behavior of the disk comparable to a coin rolled on the surface of a table. This example shows that systems with a combination of holonomic and non-holonomic constraints can be realistically modeled using this method.

3.2 Sensor calibration

The sensors in the bicycle experimental setup were first calibrated. The calibration steps of the inclinometer was programmed into the Arduino Due board. It was done by tilting the bike in all directions to the maximum extent while the program collected the maximum angles to calibrate the sensors. The rotary encoders were also calibrated through the Arduino program using the minimum and maximum sensor readings. The calibration of the strain gauges was more complex. Calibration needed to be done for forces in all three directions - normal, lateral and longitudinal. The tire-forces in lateral direction are of prime focus. Therefore the contact-point between the front wheel and the ground was first marked. Then the bicycle fork was disassembled out of the bicycle frame and supported on a vice horizontally. Various known loads were hung at the marked wheel-ground point of contact as shown in Figure 15. The readings for four strain gauges (front left, rear left, front right, rear right) were taken for loads ranging from 0-70.9N. The wheel was held horizontally and loaded – once with right side up and once with left side up. Each load (objects of different weights) was loaded and unloaded a few times for different sets of same load readings (loading and unloading cases). 20 samples were taken for every reading corresponding to each load.

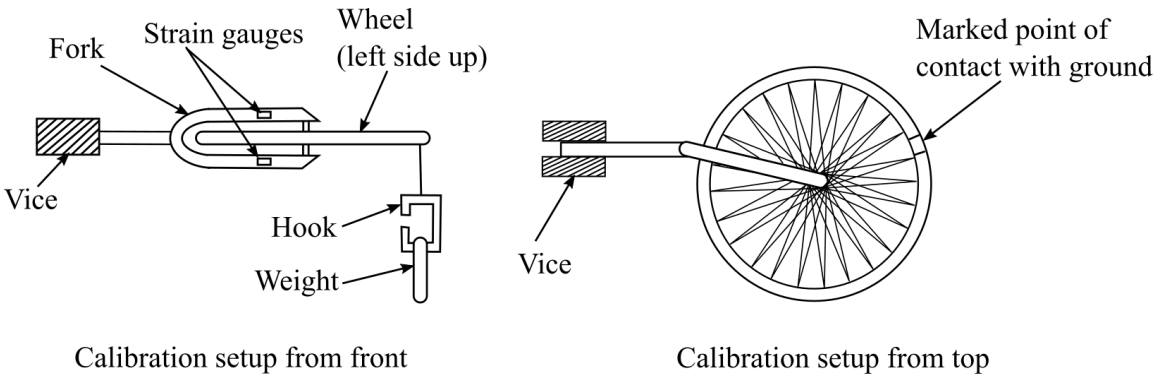

Figure 15. Strain gauge calibration setup.

The plot of readings from the front left strain gauge against applied loads when the right side of the wheel was facing up is shown in Figure 16. Ideally the plot should be stepped, increasing/decreasing with each load. Although the overall slope can be seen as increasing/decreasing in some of the plots it is not increasing/decreasing with every different

load. Plots for the other gauges show similar results. So it can be said that the readings are not accurate. In some cases lower loads display higher readings and vice versa. Precision is low as there are large variations in readings for same load. The gauge is not sensitive enough as there is small difference in readings for different loads.

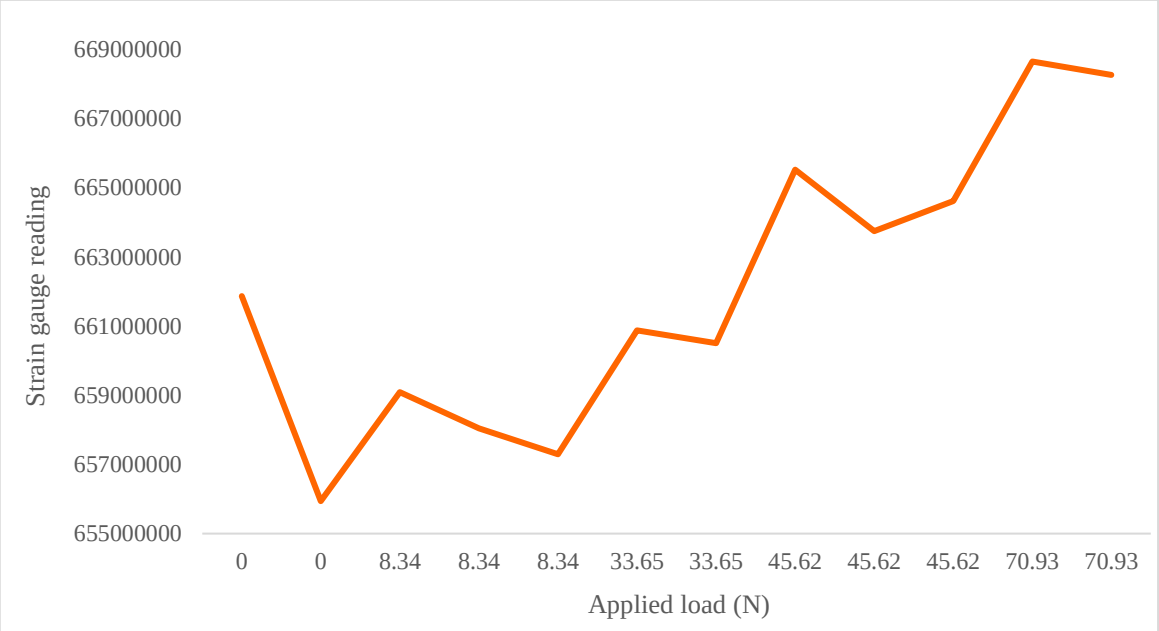

Figure 16. Front left strain gauge readings plotted against applied loads.

Figure 17 shows a more detailed plot of the 20 samples taken for the front left gauge in the first set of loading when the right side of the wheel was facing up. It is evident from the plot that the readings for different loads are overlapping with each other heavily. There is too much noise in the signal to get steady values for each load that could be differentiated from one another.

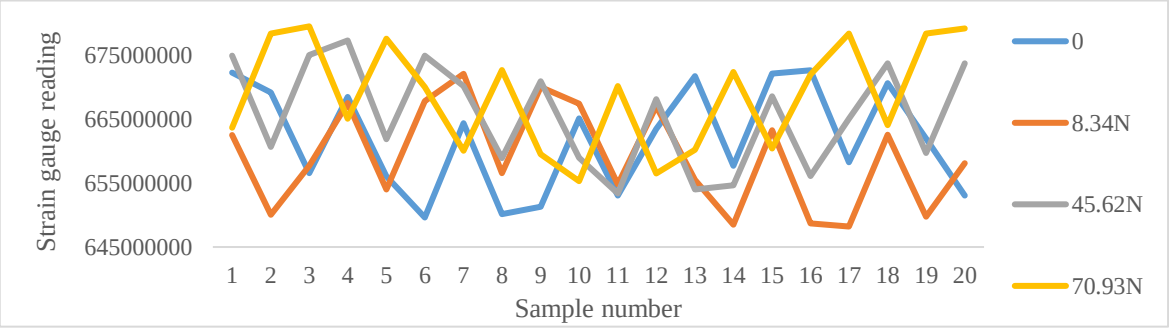

Figure 17. Plot of the 20 samples taken for the front left gauge in the first set of loading when the right side of the wheel was facing up.

The reason behind these erroneous readings is the position and alignment of the strain gauges which are optimal for normal force readings. The gauges are also capable of measuring longitudinal forces with proper amplification. But they have no sensitivity in the direction of the lateral forces. Since the most important values to be measured for this study are the lateral forces, more strain gauges are required with proper placement so that even small values of forces can be measured in the lateral direction. Assuming the fork as a cantilever beam, the value of strain at the bottom of the steerer tube where the fork splits was calculated for a load of 70.9N. This is the location where the bending moment will be maximum and result in maximum strain. The value came out to be 4.67E-7 which is an extremely small value. While it is within the measurable range of the strain gauges, one-fifth of the output signal from the analog to digital converter for this small a value is expected to be noise. This would result in unreliable results again. Therefore, simply placing new strain gauges would not solve the calibration problem. Some modifications need to be made to the bicycle fork to reduce the stiffness and maximize the measurable strain.

The modifications planned for the fork are shown in Figure 18. The steerer tube is to be cut right above the fork blades. A rectangular block is to be welded into the steerer tube joining the cut parts. Strain gauges are to be installed on the sides of this block to obtain better readings. However, these modifications have been moved out of the scope of this research work. As the most important lateral tire-forces cannot be measured the forces estimated by the inverse dynamic simulation will not be validated. The estimations will be analyzed to understand if they are realistic.

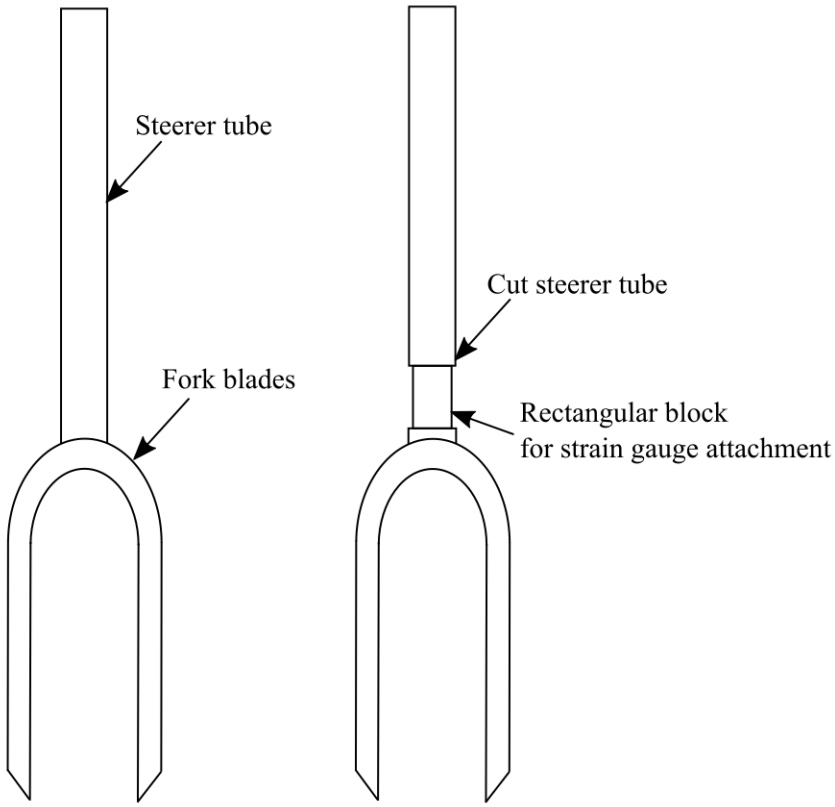

Figure 18. Modification plan for bicycle fork. The original fork is on the left and the proposed modified fork is on the right.

3.3 Inverse dynamic simulation

To obtain the dynamic coordinates of the bicycle for inverse dynamic simulation the bicycle was taken for a ride during which data from the rotary encoders and the inclinometer were recorded. This experimental data was obtained from Escalona et al. (2018, pp. 1-23). The IMU data was not used since its purpose is only to validate the kinematic analysis which is not within the scope of this study.

Figure 19 shows the trajectory of the contact-point between the ground and the rear wheel on the $\langle XY \rangle$ plane. As reflected by the plot, the bicycle was driven straight for a short while and then turned slightly left. The rider then makes a sharp U-turn towards the left. Then, after going straight for a short while the rider again takes a sharp U-turn towards the left and stops.

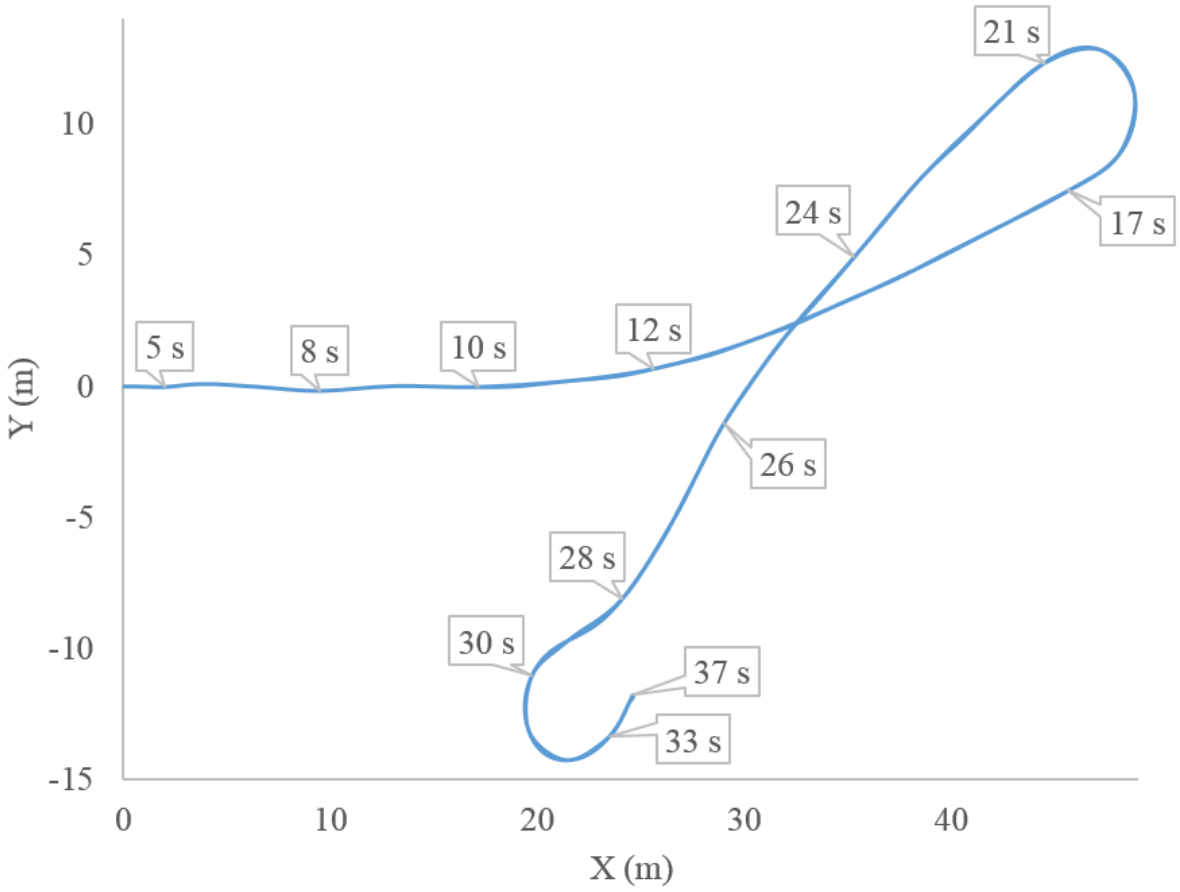

Figure 19. Trajectory of the contact-point between the ground and the rear wheel labelled with corresponding time.

The rider and bicycle model was simulated for this ride using inverse dynamic analysis with the obtained angles of lean, roll and steer. Acting as the driving actions taken by the rider these inputs yield the position of the whole bicycle model for the whole ride. The rider starts out on a straight path and turns slightly left at time 12 seconds. He then takes a U-turn from time 17 to 21 seconds. At time 26 seconds he slows down for a second U-turn which starts at time 28 and ends at 33 seconds. After that he brakes and stops the bike at time 37 seconds. This was seen in the form of an animation an image of which at time 19 seconds is shown in Figure 20. The simulation looks realistic and is an accurate reproduction of the path taken by the rider. The animation shows the rider going straight and making two sharp U-turns as corroborated by the rear wheel trajectory.

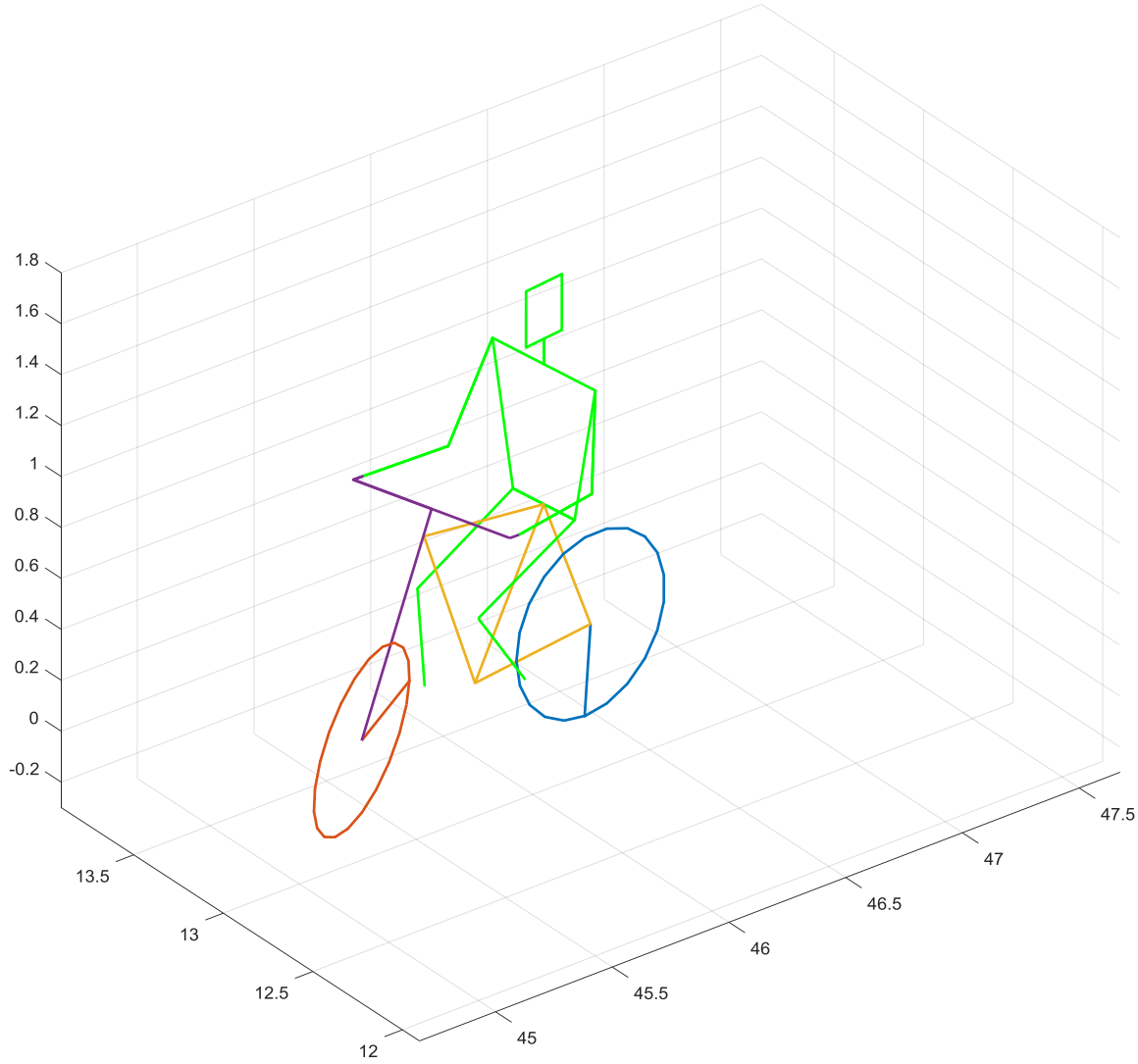

Figure 20. Image of bicycle ride simulation taken at time 19 seconds when the rider is taking the first U-turn.

3.4 Driving forces

The Lagrange multiplier λ_9 represents the driving forces associated with the mobility constraint for steering angle. This means that λ_9 gives the values for steering torque. Figure 21 shows the plot for steering torque over time. From the beginning of the ride to time 17 seconds the steering torque fluctuates around zero due to natural wobbling of the steering assembly for stability. It rises after that as the bicycle turns left up to 9Nm until time 21 seconds following which the rider takes a straight path again. Consequently, the fluctuation about zero reappears until at time 28 seconds the rider makes a U-turn again raising the

steering torque to 7Nm. This shows that the behavior of the steering torque simulated by the model accurately represents the rider's behavior.

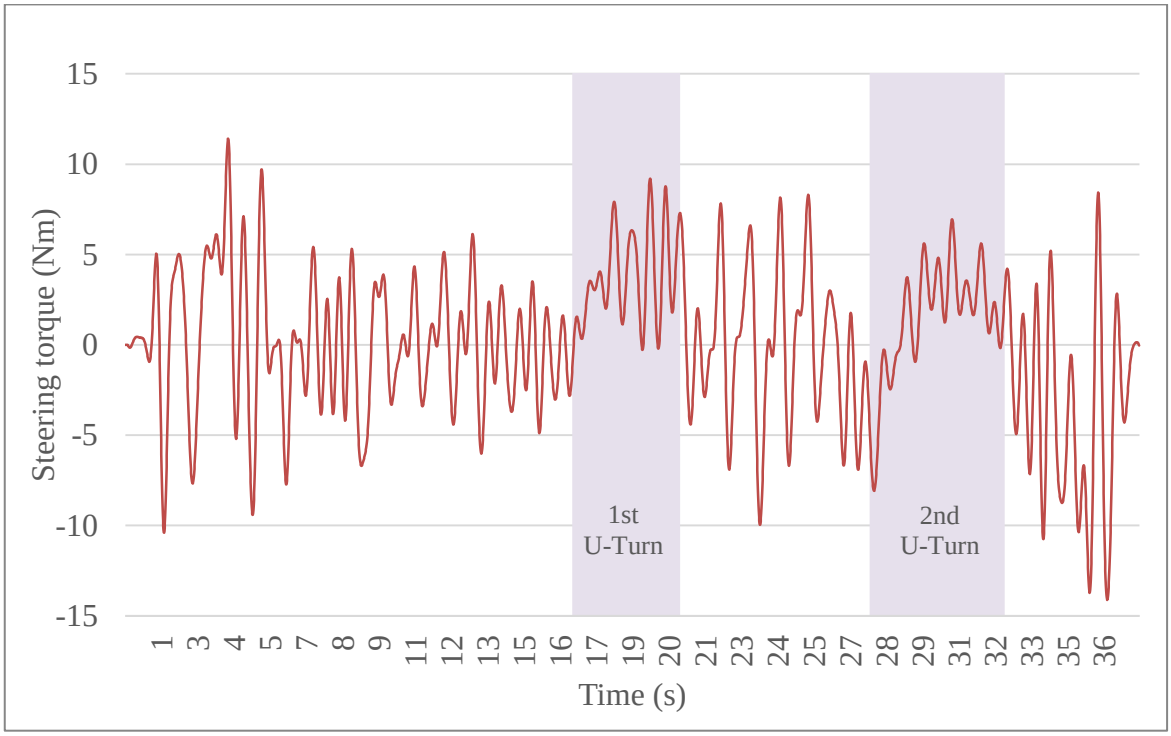

Figure 21. Plot of steering torque over time.

The Lagrange multiplier λ_8 represents the driving forces associated with the mobility constraint for the rear wheel roll angle. This implies that λ_8 indicates values for pedaling torque. Figure 22 shows the plot for pedaling torque over time. It is difficult to speculate the behavior of pedaling torque applied by the rider by knowing the path alone. However, the small spike in the torque at the beginning of the ride clearly indicates the torque applied to start the bike. For the most part the pedaling toque is positive, because of the rider's need to pedal to keep the bike running. When the rider takes the first U-turn at time 17 seconds a sudden and brief drop in the pedaling torque is noticed as the rider slows down for the turn. Again at time 26 seconds the pedaling torque starts dropping as the rider slows down for the second U-turn. Towards the end of the ride at time 33 seconds there is an even sharper drop due to braking torque following which there is slight pedaling and braking again. This is due to the rider pressing the brakes twice to stop the bike.

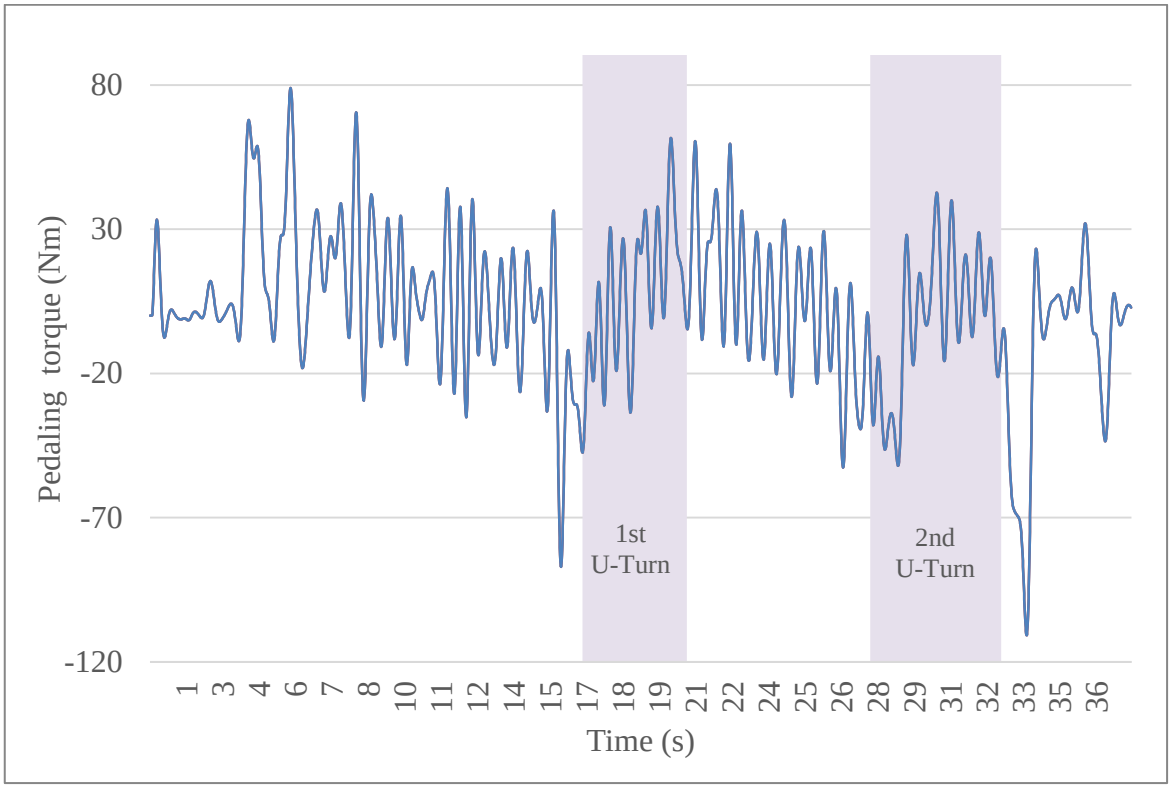

Figure 22. Plot of pedaling torque over time.

The Lagrange multiplier λ_7 represents the forces associated with the mobility constraint for the rear wheel lean angle. This implies that λ_7 indicates the values for leaning torque. Escalona et al. (2018, pp. 1-23) consider this Lagrange multiplier to be proof that this bicycle model is not an accurate representation of the real ride because the model cannot describe relative leaning between the rider and the bicycle frame and so λ_7 cannot depict the leaning torque. However, Kooijman et al. (2011, pp. 339-342) have investigated the reasons for stability of a bicycle noting that leaning can induce steering in a bike and how riders often use leaning as a way to steer when riding hands-free. This indicates possible application of leaning torque by the rider to balance the bike by inducing steering. Since the application of leaning torque by the rider cannot be characterized by taking note of the path or even by experimental measures, the estimated leaning torques have no meaning in this study.

3.5 Tire-road forces

The Lagrange multipliers λ_1, λ_3, λ_4, λ_5 and λ_6 give us the values of the tire-road forces. The reaction forces acting on the tire of any vehicle are shown in Figure 23. The estimation of these forces for the bicycle is the main result of this research work.

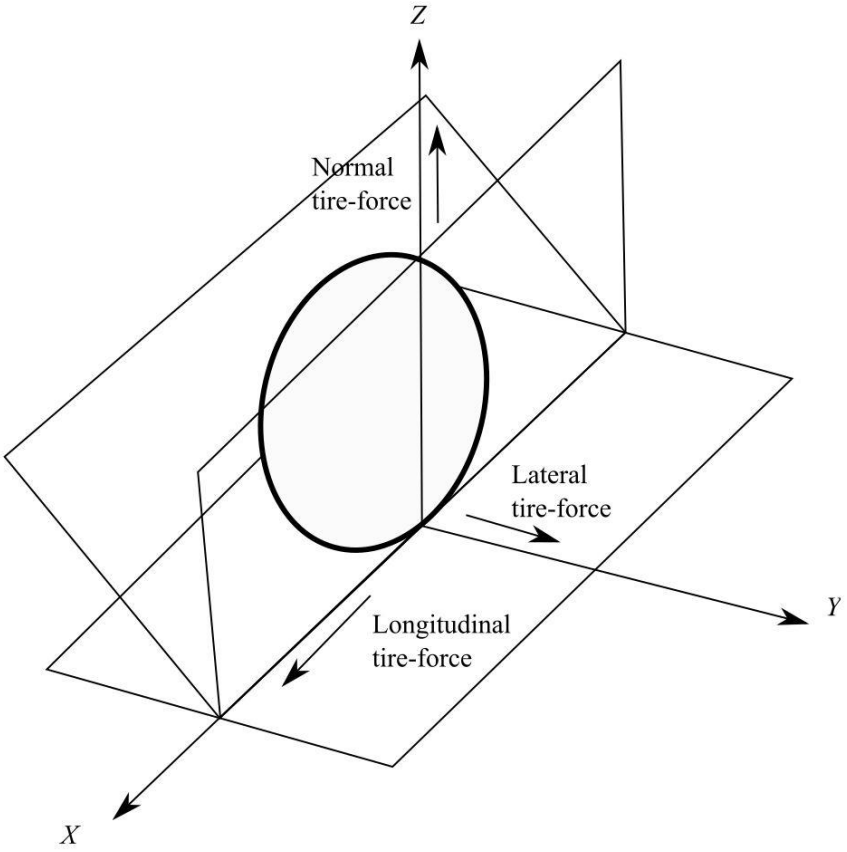

Figure 23. Reaction forces acting on the tire (mod. Rajamani, 2014, p. 356).

The Lagrange multiplier λ_1 is associated with the first contact constraint applied to the front wheel which represents the tire-force at the front wheel in normal direction. Figure 24 shows the plot of this normal-tire force with time. The force fluctuates around 200N indicating the part of the weight of the cyclist and bike that is borne by the front wheel. The U-turns have been taken from time 17 to 21 seconds and from time 28 to 33 seconds. During these U-turns the rider slows the bike down. The rider also applies the brake at the end of the ride at time 33 seconds to stop the bike. The normal tire forces can be seen to rise during these U-turns and again more sharply at the end of ride. These increases in the normal tire-forces relate to braking situations when greater portion of the load is shifted to the front wheel.

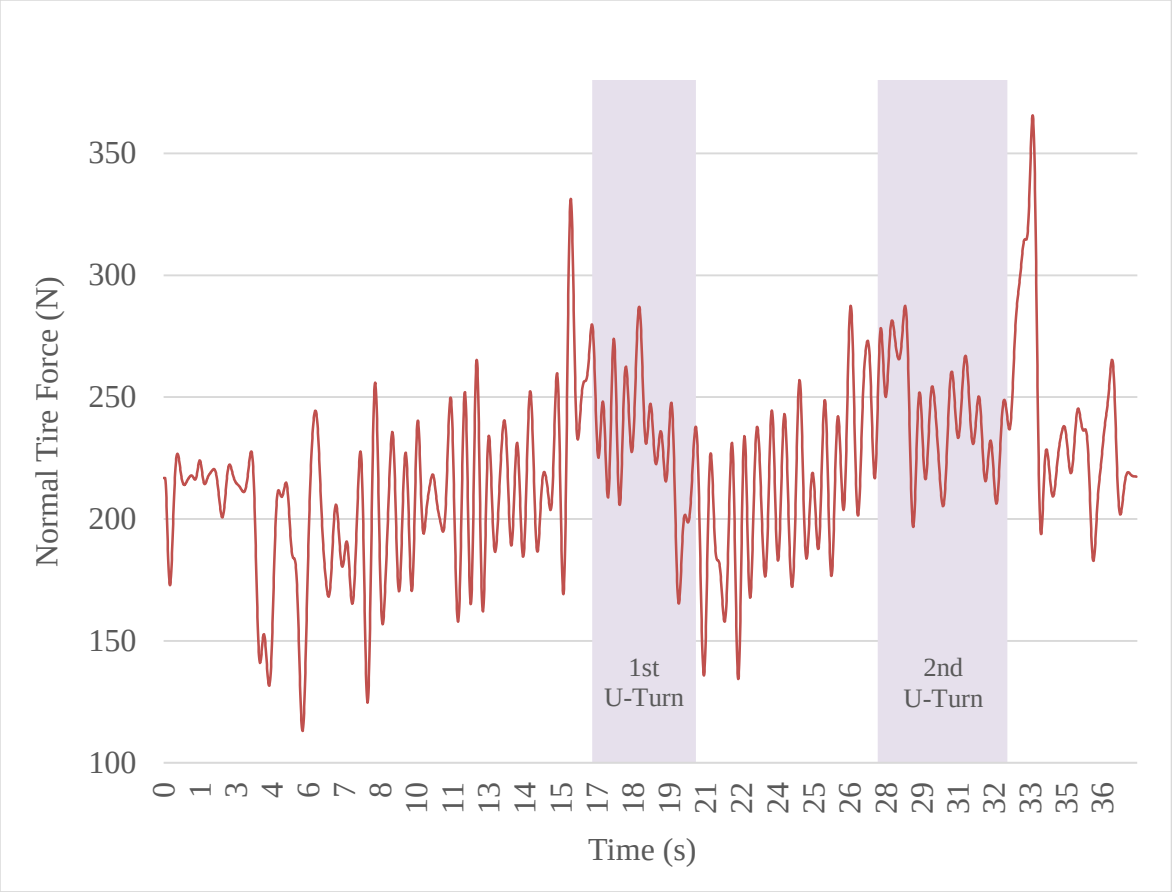

Figure 24. Plot of normal tire-force at the front wheel over time.

The longitudinal tire-forces acting on the rear wheel are given by λ_3 and those acting on the front wheel are given by λ_5 as these Lagrange multipliers are related to the rolling-without-slipping constraints. They have been plotted against time in Figure 25. The longitudinal forces depend on the tire-road friction coefficient, normal tire-force and the longitudinal slip ratio (Rajamani, 2014, pp. 1-11). As this model is based on rolling-without-slipping constraints with no change in the experimental ride surface friction, the longitudinal forces are dependent on the normal forces alone. This is reflected in the obtained plot as the longitudinal forces fluctuate around zero while the path is straight and rise or fall when the rider takes U-turns which is the time when the normal forces rise due to braking. The U-turns are depicted in the longitudinal force plot as successive rise and fall or vice versa for each U-turn. This is because the forces are obtained in the global frame and as the rider takes a U-turn the direction of the longitudinal forces become opposite.

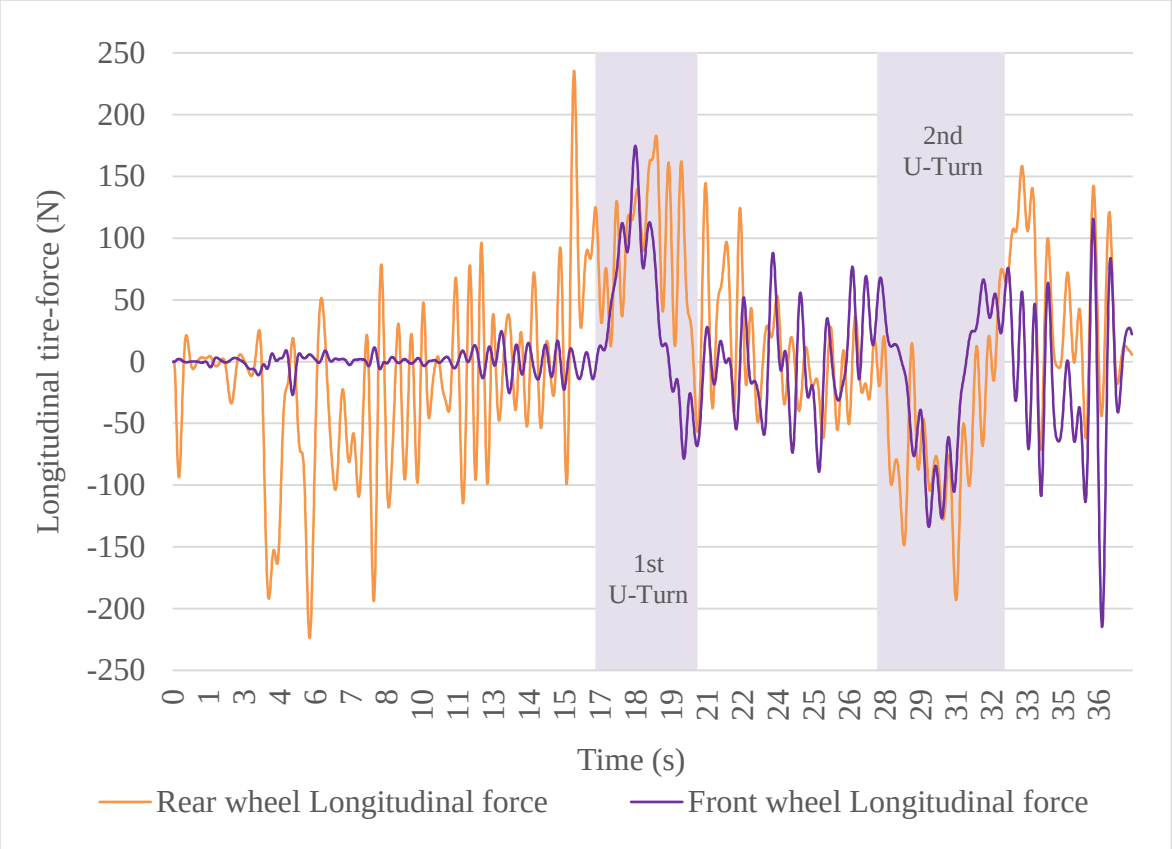

Figure 25. Plot of the front and rear wheel longitudinal tire-forces over time.

The Lagrange multipliers λ_4 and λ_6 represent the rear wheel lateral tire-forces and the front wheel lateral tire-forces, respectively as these Lagrange multipliers are related to the rolling-without-slipping constraints. Figure 26 shows the plot of these forces against time. The lateral forces experienced by both wheels are similar except for a spike in the rear wheel lateral force towards the end of the ride. This is an effect of the braking torque experienced in the form of lateral force by the rear wheel due to braking in the turning position. The remaining plot shows the fluctuation about zero for the straight path during which there is no lateral force because the rolling-without-slipping constraints eliminate the sideslip phenomenon. Even in the experiment there is no sideslip expected as the tire-road conditions are not slippery. During the U-turn the lateral tire-forces rise and fall or vice versa due to centrifugal and Coriolis forces. There is an additional drop before the second U-turn starting at time 26 seconds induced by the slight steering before the U-turn as seen in the rear wheel trajectory (Figure 19). The U-turns are described by a combination of rise and fall in the magnitude of the Lagrange multipliers because just like the longitudinal forces, the lateral forces are also obtained in the global frame resulting in a sign change during U-turns.

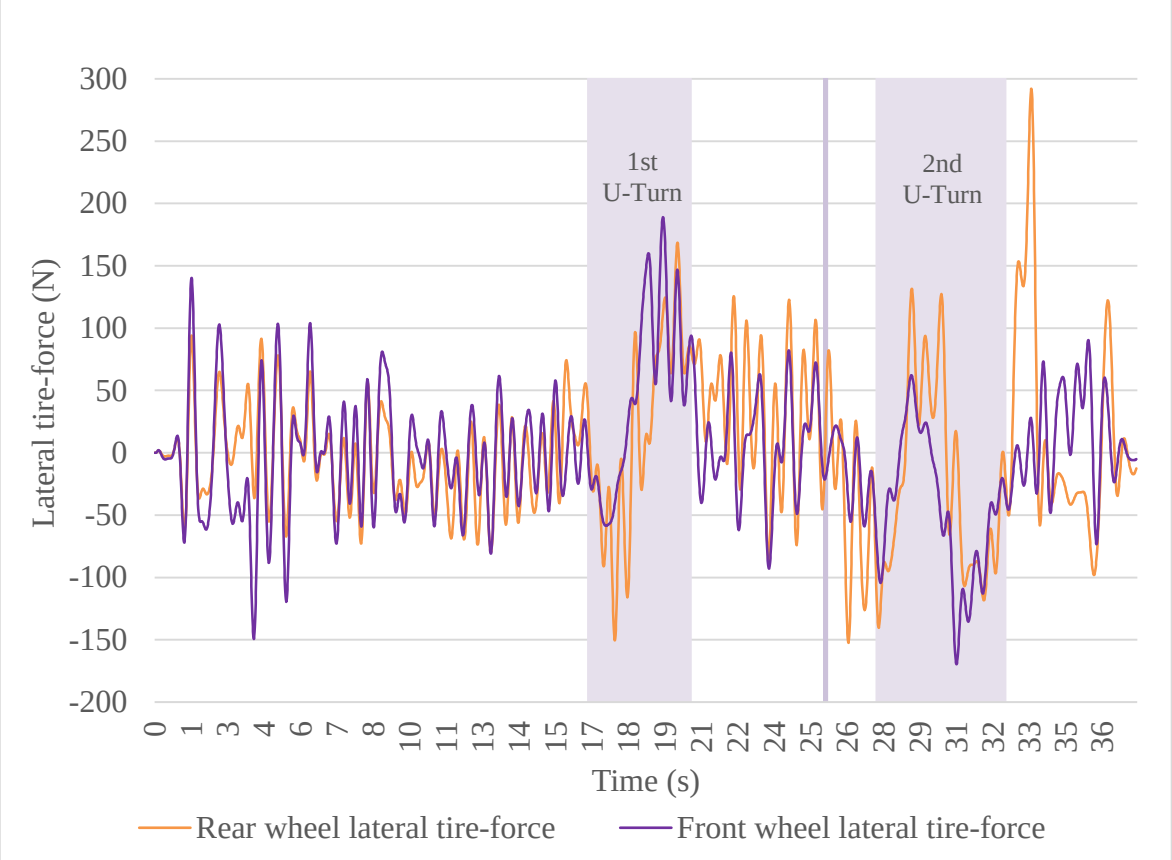

Figure 26. Plot of front and rear wheel lateral tire-forces over time.

4 DISCUSSION

A multibody bicycle model has been used in this research work to estimate the tire-forces through Lagrange multipliers obtained from inverse dynamic analysis. The bicycle model was designed using rolling-without-slipping constraints and is meant to provide a starting point for simulation models of four-wheeled vehicles that can estimate tire-forces for vehicle handling and stability systems.

The results obtained with this model are the driving forces and the tire-road forces. The driving forces comprise of the steering torque, pedaling torque and the leaning torque. Both steering torque and pedaling torque accurately represent the rider's actions. However, the interpretation of the leaning torque is unclear. The tire-road forces are the most important results of this study. The only factor affecting the longitudinal forces is the normal tire-force and their behavior correspond to each other. The lateral tire-forces also relate to the turning of the bicycle and is sensitive to cornering in even small curvatures. These tangential forces, however, do not account for the effects of slipping and as the model is designed for rolling-without-slipping.

The tire-road forces obtained in this study are highly relevant to stability systems for bicycles. Such systems are useful for electric bikes, bikes for elderly people and other advanced bicycle applications. Good estimations have been achieved with simple and inexpensive sensors, making this a viable option for commercial application. The additional results of driving forces can also be useful as they provide information that the riders might be interested in.

Some of the assumptions made in the model, though, reduce its applicability to vehicle handling systems. The first such assumption is the knife-edge wheel that makes point contact with the ground. In a realistic tire model, especially car tires, there is a whole patch of area that makes contact with the ground. A surface contact model is required to make this model more realistic. The second assumption is the lack of slipping phenomenon. In a realistic vehicle, the slipping is an important factor in the variation of tire-forces and a major cause of stability issues which calls for stability control systems. By making the assumption of

rolling-without-slipping the efficacy of the model during slipping of the wheels cannot be analyzed. Experimental validation, which was initially planned within the scope of this research, was not performed because of which the level of accuracy achieved by the model could not be judged.

Although there are some shortcomings of this model, the main objective of this study, which was to create a multibody model of a bicycle which can accurately estimate the tire-road forces using a minimal set of sensors, has been achieved. The results and analysis reveal how the patterns of tire-road forces estimated co-relate to the factors affecting them. The sensors used were the most basic compared to sensors used in current commercialized systems and research work in this area. This bicycle model is definitely a starting point for developing more complex and realistic models of four-wheeled vehicles that can eventually be applied to commercial vehicle handling systems.

In the future, the tire-force estimations made by this bicycle model must be experimentally validated by modifying the bicycle to get accurate and precise strain gauge readings. The assumptions in the model should be removed for a more realistic simulation. This primarily includes replacing the rolling-without-slipping constraints with constraints accounting for sideslip and longitudinal slip. Another important aspect is to introduce a surface contact model instead of point contact using voluminous wheels so as it to make it resemble four-wheeled vehicles more. After making these modification to the simulation model, it should be experimentally verified by riding the bicycle on roads having variable road friction. The robustness of the model against changes in tire-road parameters is an important factor in this topic of research. Once a bicycle model that simulates realistic behavior of the bike using just the minimal set of sensors as used here against varying outside parameters is developed it has to be expanded into a four-wheel vehicle model. An observer using Kalman filter can then be combined with it to act as a virtual sensor. Therefore, the future scope of this research work can be listed as follows:

1. Experimental validation of tire-force estimations of current model.
2. Development of a more realistic model by including slip phenomenon.
3. Developing tire surface contact model for resemblance to four-wheel vehicle tires.
4. Experimental validation with varying road conditions

5. Expansion of the model to a four-wheeled vehicle.
6. Addition of a dynamic observer to the vehicle model.

Accurately estimating the tire-road forces through a multibody vehicle model taking inputs from sensors measuring just the geometrical parameters would be of great scientific contribution. It will eliminate the necessity of the numerous sensors used in cars currently and make vehicle handling systems available on non-luxury car models. By making vehicle safety systems more affordable the accident rates can be reduced considerably.

5 CONCLUSION

This study is about the development of a multibody bicycle model that can estimate the tire-road forces. One of the main parameters required by vehicle stability control systems these days is the lateral tire-force. Many control systems are available currently in luxury cars but they use expensive sensors or require prior knowledge of tire and road conditions. This research work aimed at building an accurate dynamic model of a bicycle which can estimate tire-road forces of a vehicle using a minimal set of sensors. The bicycle was chosen instead of a four wheeled model as it is a simpler vehicle with many dynamic properties. The main research question was whether the proposed bicycle model can provide a starting point for four-wheel vehicle tire-force estimators that could be feasible for application in commercialized vehicle handling systems or not.

The numerical example of a three dimensional rolling disk was first simulated. It showed that the selected method produces realistic simulations of non-holonomic systems. The bicycle model's equations of motion were then derived. The bicycle model was simulated using inverse dynamic analysis taking the rider's actions as input for the model. This involved the usage of only an inclinometer and two rotary encoders. The Lagrange multipliers obtained from the solution of the equations of motion were interpreted as the driving and the reaction forces. Their plots showed that the patterns of the obtained forces represent the accurate behavior of the bicycle.

These results have demonstrated that this bicycle model could be expanded into a four-wheeled model which would be suitable for commercial use in control systems used in vehicles due to the minimal requirement of sensors and realistic results. Experimental validation of the tire-force estimates were removed from the scope of the research as the installed strain gauges could not measure the most important lateral forces. Modifications to the experimental setup have been suggested to obtain the measurements necessary for complete validation.

The validation is the immediate topic for future research following which some of the assumptions in the current model need to be removed for a more realistic simulation

appropriate for four-wheeled vehicles. After these enhancements in the model it should be validated against varying road conditions after which a four-wheeled model can be developed. The addition of a Kalman filter based dynamic observer to the model has also been discussed in this research work as a future scope.

LIST OF REFERENCES

Aga, M. and Okada, A. (2003) Analysis of vehicle stability control (VSC)'s effectiveness from accident data, *International Technical Conference on the Enhanced Safety of Vehicles, National Highway Traffic Safety Administration*, p. 7.

Baffet, G., Charara, A. and Lechner, D. (2009) Estimation of vehicle sideslip, tire force and wheel cornering stiffness, *Control Engineering Practice*, 17(11), pp. 1255-1264.

Bakker, E., Nyborg, L. and Pacejka, H.B. (1987) Tyre modelling for use in vehicle dynamics studies, *SAE Transactions*, pp. 190-204.

Boukattaya, M., Mezghani, N. and Damak, T. (2018) Adaptive motion/force control of uncertain nonholonomic mobile manipulator with estimation of unknown external force, *Multibody System Dynamics*, pp. 1-28.

Cho, W., Yoon, J., Yim, S., Koo, B. and Yi, K. (2010) Estimation of tire forces for application to vehicle stability control, *IEEE Transactions on Vehicular Technology*, 59(2), pp. 638-649.

Dang, J.N. (2004) Preliminary results analyzing the effectiveness of electronic stability control (ESC) systems, *US Department of Transportation, National Highway Traffic Safety Administration*, p. 4.

Dao, T.K. and Chen, C.K. (2012) A study of bicycle dynamics via system identification approaches, *Journal of the Chinese Institute of Engineers*, 35(7), pp. 853-868.

Doumiati, M., Victorino, A., Charara, A. and Lechner, D. (2009) Estimation of vehicle lateral tire-road forces: a comparison between extended and unscented Kalman filtering, *In Control Conference (ECC), 2009 European, IEEE*, pp. 4804-4809.

Escalona, J.L. and Recuero, A.M. (2012) A bicycle model for education in multibody dynamics and real-time interactive simulation, *Multibody System Dynamics*, 27(3), pp. 383-402.

Escalona, J.L., Kłodowski, A. and Muñoz, S. (2018) Validation of multibody modeling and simulation using an instrumented bicycle: from the computer to the road, *Multibody System Dynamics*, pp. 1-23.

Ghoneim, Y.A., Lin, W.C., Sidlosky, D.M., Chen, H.H. and Chin, Y.K. (2000) Integrated chassis control system to enhance vehicle stability, *International Journal of Vehicle Design*, 23(1-2), pp. 124-144.

Goldstein, H. (1950) *Classical mechanics*. 1st edn. Cambridge, MA: Addison-Wesley. pp. 16-22.

Grewal, M.S., Andrews, A.P. and Bass, R.W. (1995) Kalman filtering: Theory and practice, *IEEE Transactions on Automatic Control*, 40(11), p. 1983.

Hoffman, D.D. and Rizzo, M.D. (1998) Chevrolet C5 Corvette vehicle dynamic control system, *SAE Technical Paper*, pp. 1-3.

Jung, H. and Choi, S.B. (2018) Real-time individual tire force estimation for an all-wheel drive vehicle, *IEEE Transactions on Vehicular Technology*, 67(4), pp. 2934-2944.

Kin, K., Yano, O. and Urabe, H. (2003) Enhancements in vehicle stability and steerability with slip control, *JSAE review*, 24(1), pp. 71-79.

Kooijman, J.D.G., Meijaard, J.P., Papadopoulos, J.M., Ruina, A. and Schwab, A.L. (2011) A bicycle can be self-stable without gyroscopic or caster effects, *Science*, 332(6027), pp. 339-342.

Lee, H. and Tomizuka, M. (2003) Adaptive vehicle traction force control for intelligent vehicle highway systems (IVHSs), *IEEE Transactions on Industrial Electronics*, 50(1), pp. 37-47.

Leffler, H., Auffhammer, R., Heyken, R. and Röth, H. (1998) New driving stability control system with reduced technical effort for compact and medium class passenger cars, *SAE Technical Paper*, pp. 1-3.

Lie, A., Tingvall, C., Krafft, M. and Kullgren, A. (2004) The effectiveness of ESP (electronic stability program) in reducing real life accidents, *Traffic Injury Prevention*, 5(1), pp. 37-41.

Lie, A., Tingvall, C., Krafft, M. and Kullgren, A. (2006) The effectiveness of electronic stability control (ESC) in reducing real life crashes and injuries, *Traffic injury prevention*, 7(1), pp. 38-43.

Meijaard, J.P., Papadopoulos, J.M., Ruina, A. and Schwab, A.L. (2007) Linearized dynamics equations for the balance and steer of a bicycle: a benchmark and review, *Proceedings of the Royal society A: mathematical, physical and engineering sciences*, 463(2084), pp. 1955-1982.

Nam, K., Fujimoto, H. and Hori, Y. (2012) Lateral stability control of in-wheel-motor-driven electric vehicles based on sideslip angle estimation using lateral tire force sensors, *IEEE Transactions on Vehicular Technology*, 61(5), pp. 1972-1985.

Nam, K., Hori, Y. and Lee, C. (2015) Wheel slip control for improving traction-ability and energy efficiency of a personal electric vehicle, *Energies*, 8(7), pp. 6820-6840.

Nam, K., Oh, S., Fujimoto, H. and Hori, Y. (2013) Estimation of sideslip and roll angles of electric vehicles using lateral tire force sensors through RLS and Kalman filter approaches, *IEEE Transactions on Industrial Electronics*, 60(3), pp. 988-1000.

National Highway Traffic Safety Administration. (2016) *Traffic safety facts 2015*. 1st edn. Washington, DC: Department of Transportation, National Highway Traffic Safety Administration. pp. 1-11.

National Highway Traffic Safety Administration. (2018) *Traffic safety facts 2016*. 1st edn. Washington, DC: Department of Transportation, National Highway Traffic Safety Administration. pp. 1-11.

Ono, E., Asano, K., Sugai, M., Ito, S., Yamamoto, M., Sawada, M. and Yasui, Y. (2003) Estimation of automotive tire force characteristics using wheel velocity, *Control engineering practice*, 11(12), pp. 1361-1370.

Ono, K., Takizawa, T. and Aoki, M., NSK Ltd, (2014) *Preload measuring device for double row rolling bearing unit*, U.S. Patent 8864382, pp. 21-22.

Rajamani, R. (2011) *Vehicle dynamics and control*. 2nd edn. Springer Science & Business Media. pp. 1-11.

Ray, L.R., (1995) Nonlinear state and tire force estimation for advanced vehicle control, *IEEE Transactions on control systems technology*, 3(1), pp. 117-124.

Ray, L.R. (1997) Nonlinear tire force estimation and road friction identification: Simulation and experiments, *Automatica*, 33(10), pp. 1819-1833.

Rezaeian, A., Zarringhalam, R., Fallah, S., Melek, W.W., Khajepour, A., Chen, S.K., Moshchuck, N. and Litkouhi, B. (2015) Novel Tire Force Estimation Strategy for Real-Time Implementation on Vehicle Applications, *IEEE Trans. Vehicular Technology*, 64(6), pp. 2231-2241.

Sanjurjo, E., Dopico, D., Luaces, A. and Naya, M.Á. (2018) State and force observers based on multibody models and the indirect Kalman filter, *Mechanical Systems and Signal Processing*, 106, pp. 210-228.

Schwab, A.L. and Meijaard, J.P. (2013) A review on bicycle dynamics and rider control, *Vehicle System Dynamics*, 51(7), pp. 1059-1090.

Schwab, A.L., Kooijman, J.D.G. and Nieuwendijk, J. (2012) On the design of a recumbent bicycle with a perspective on handling qualities, *ASME 2012 International Design Engineering Technical Conferences and Computers and Information in Engineering Conference*, American Society of Mechanical Engineers, pp. 303-308.

Schwab, A.L. (2014) On the Interpretation of the Lagrange Multipliers in the Constraint Formulation of Contact Problems; or Why Are Some Multipliers Always Zero? *In ASME 2014 International Design Engineering Technical Conferences and Computers and Information in Engineering Conference*, American Society of Mechanical Engineers, pp. 22-27.

Schwab, A.L., Meijaard, J.P. and Papadopoulos, J.M. (2005) A multibody dynamics benchmark on the equations of motion of an uncontrolled bicycle, *In Proceedings of the Fifth EUROMECH Nonlinear Dynamics Conference, ENOC-2005*, Eindhoven University of Technology, The Netherlands, pp. 511-521.

Scopus. (2018) *Analyze search results* [online]. Available at: https://www-scopus-com.ezproxy.cc.lut.fi/term/analyzer.uri?sid=2c188ba524db3664c8ad87275d76c612&origin=resultslist&src=s&s=TITLE-ABS-KEY%28%22tire-force%22+and+%22estimation%22%29&sort=plf-f&sdt=b&sot=b&sl=44&count=357&analyzeResults=Analyze+results&txGid=388a8e71f648112847100d5e1d3050e0 (Accessed 15 Dec. 2018).

Shabana, A.A. and Sany, J.R. (2001) An augmented formulation for mechanical systems with non-generalized coordinates: application to rigid body contact problems, *Nonlinear dynamics*, 24(2), pp. 183-204.

Shabana, A.A. (2013) *Dynamics of multibody systems*. 3rd edn. Cambridge university press. pp. 85-156.

Sharp, R.S. (2008) On the stability and control of the bicycle, *Applied mechanics reviews*, 61(6), pp. 1-24.

Strassberger, M. and Guldner, J. (2004) BMW's dynamic drive: an active stabilizer bar system, *IEEE control systems*, 24(4), pp. 28-29.

Wang, D. and Qi, F. (2001) Trajectory planning for a four-wheel-steering vehicle, *In Robotics and Automation, 2001. Proceedings 2001 ICRA. IEEE International Conference on. IEEE*, 4, pp. 3320-3325.

Whipple, F.J. (1899) The stability of the motion of a bicycle, *Quarterly Journal of Pure and Applied Mathematics*, 30(120), pp. 312-321.